Estimation of field-scale soil hydraulic and dielectric parameters through joint inversion of GPR and hydrological data

M. B. Kowalsky,[1] S. Finsterle,[1] J. Peterson,[1] S. Hubbard,[1] Y. Rubin,[2] E. Majer,[1] A. Ward,[3] and G. Gee[3]

[1]   A method is described for the joint use of time-lapse ground-penetrating radar (GPR) travel times and hydrological data to estimate field-scale soil hydraulic parameters. We build upon previous work to take advantage of a wide range of cross-borehole GPR data acquisition configurations and to accommodate uncertainty in the petrophysical function, which relates soil porosity and water saturation to the effective dielectric constant. We first test the inversion methodology using synthetic examples of water injection in the vadose zone. Realistic errors in the petrophysical function result in substantial errors in soil hydraulic parameter estimates, but such errors are minimized through simultaneous estimation of petrophysical parameters. In some cases the use of a simplified GPR simulator causes systematic errors in calculated travel times; simultaneous estimation of a single correction parameter sufficiently reduces the impact of these errors. We also apply the method to the U.S. Department of Energy (DOE) Hanford site in Washington, where time-lapse GPR and neutron probe (NP) data sets were collected during an infiltration experiment. We find that inclusion of GPR data in the inversion procedure allows for improved predictions of water content, compared to predictions made using NP data alone. These examples demonstrate that the complimentary information contained in geophysical and hydrological data can be successfully extracted in a joint inversion approach. Moreover, since the generation of tomograms is not required, the amount of GPR data required for analyses is relatively low, and difficulties inherent to tomography methods are alleviated. Finally, the approach provides a means to capture the properties and system state of heterogeneous soil, both of which are crucial for assessing and predicting subsurface flow and contaminant transport.

Citation: Kowalsky, M. B., S. Finsterle, J. Peterson, S. Hubbard, Y. Rubin, E. Majer, A. Ward, and G. Gee (2005), Estimation of field-scale soil hydraulic and dielectric parameters through joint inversion of GPR and hydrological data, *Water Resour. Res.*, *41*, W11425, doi:10.1029/2005WR004237.

1.   Introduction

[2]   Ground-penetrating radar (GPR) measurements are not directly related to soil hydraulic parameters in the vadose zone. However, they are highly sensitive to fluid distribution (and changes thereof) and are therefore potentially useful for inferring soil hydraulic parameters. The use of GPR methods for characterizing the distribution and movement of fluids in the subsurface is well established. However, only recently has the potential for using time-lapse GPR measurements to infer soil hydraulic properties—which can then be used to model flow and transport—been explored [*Binley et al.*, 2002; *Kowalsky*, 2003; *Kowalsky et al.*, 2004a; *Lambot et al.*, 2004; *Rucker and Ferré*, 2004]. The response of a hydrological system to external stimuli, such as the injection of water in the subsurface or ponding of water on the ground surface, depends primarily on the soil hydraulic functions and their variations in space (and on the initial and boundary conditions). Corresponding GPR measurements of the same system also depend on the soil hydraulic functions—although indirectly—because the soil hydraulic functions influence the water distribution, which in turn influences the GPR response.

[3]   A review of GPR applications in hydrological investigations is given by *Annan* [2005]. The soil property that most directly affects the speed at which GPR waves travel in the subsurface is the dielectric permittivity. For simplicity we use the (relative) dielectric constant κ, defined as the dielectric permittivity of a material normalized by that of free space. For common earth materials and under favorable conditions (e.g., where highly conductive materials, such as clays, are sparse), the dielectric constant is related to the electromagnetic (EM) wave velocity (V) through

$$V \approx \frac{c}{\sqrt{\kappa}}, \qquad (1)$$

where c is the EM wave velocity in free space [*Davis and Annan*, 1989]. The presence of water affects the dielectric

---

[1]Earth Sciences Division, Lawrence Berkeley National Laboratory, Berkeley, California, USA.
[2]Department of Civil and Environmental Engineering, University of California, Berkeley, California, USA.
[3]Hydrology Group, Pacific Northwest National Laboratory, Richland, Washington, USA.

constant of soil mixtures [*Daniels*, 1996] in a manner that can be modeled with relationships that are purely empirical [*Topp et al.*, 1980; *Persson et al.*, 2002], semi-empirical [*Birchak et al.*, 1974; *Roth et al.*, 1990], or theoretical [*de Loor*, 1964; *Dobson et al.*, 1985; *Friedman*, 1998; *Sihvola*, 1999]. Hereafter, we refer to the functions that relate water content (or water saturation) to the dielectric constant of soil mixtures as petrophysical functions, and to the parameters that describe such functions as petrophysical parameters.

[4] Because of their high sensitivity to the pore water distribution, cross-borehole ground-penetrating radar (GPR) measurements are used increasingly for imaging transient flow in the vadose zone [e.g., *Alumbaugh et al.*, 2002; *Binley et al.*, 2001; *Kowalsky et al.*, 2004b]. Tomographic inversion techniques [*Peterson et al.*, 1985] are typically applied to cross-borehole GPR data sets [*Eppstein and Dougherty*, 1998; *Peterson*, 2001] to obtain spatial distributions of EM velocity (tomograms), which can be converted to water saturation using a petrophysical function.

[5] While tomography is especially useful for gaining a qualitative understanding of flow processes in the subsurface (e.g., to help identify preferential flow paths), there are some well known limitations, such as the occurrence of artifacts, like smoothing and smearing, that can be introduced through the tomographic inversion procedure [*Stewart*, 1991; *Peterson*, 2001]. For demonstration, Figure 1 depicts the traditional application of cross-borehole tomography for the case of a simulated water injection in the vadose zone. An injected water plume corresponds to the region with decreased EM velocity (Figure 1a). Simulation of a dense set of GPR measurements (Figure 1b), followed by tomographic inversion, results in a tomogram (Figure 1c) that is similar to the true velocity model but is distorted. An implicit assumption in such a procedure is that the water distribution, which determines the EM velocity distribution, remains constant during the survey; in reality it may change appreciably, especially in dynamic flow situations.

[6] Such limitations make the direct use of tomograms potentially problematic for hydrological applications [*Day-Lewis and Lane*, 2004; *Moysey et al.*, 2005]. A more fundamental limitation is that traditional cross-borehole tomography cannot in general be used to obtain quantitative estimates of vadose zone flow parameters, like the permeability and the soil hydraulic parameters of the capillary pressure and relative permeability functions, except in some limited cases [e.g., *Hubbard et al.*, 1997].

[7] As opposed to the typical use of cross-borehole data described above and depicted in Figure 1, an alternative application involves their direct integration in hydrological inversion schemes in a coupled fashion (i.e., where the geophysical and hydrological data are simulated simultaneously and are explicitly linked to hydrological parameters). Few such applications have been reported in the literature, especially for vadose zone applications. *Hyndman et al.* [1994] and *Hyndman and Gorelick* [1996] developed an inversion algorithm for estimating lithological zones and the hydrological parameters of the zones in fully saturated aquifers using seismic and tracer
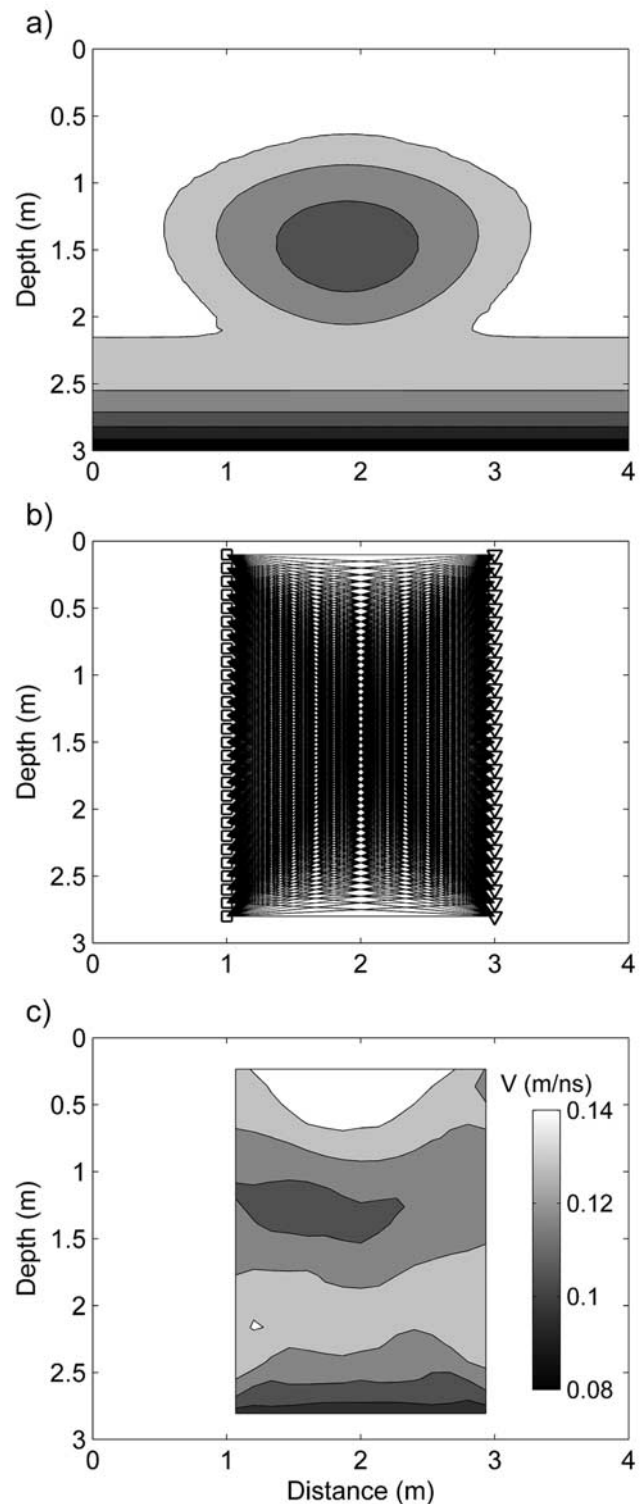

Figure 1. Traditional cross-borehole tomography using synthetic GPR measurements. For this example, a dense set of GPR measurements were simulated with a velocity model corresponding to that shown in (a) and with GPR antenna positions as indicated in (b), giving the velocity tomogram shown in (c). The color scale for velocity (V) is the same for both (a) and (c). Squares and triangles in (b) indicate the position of the transmitting and receiving antenna locations, respectively.
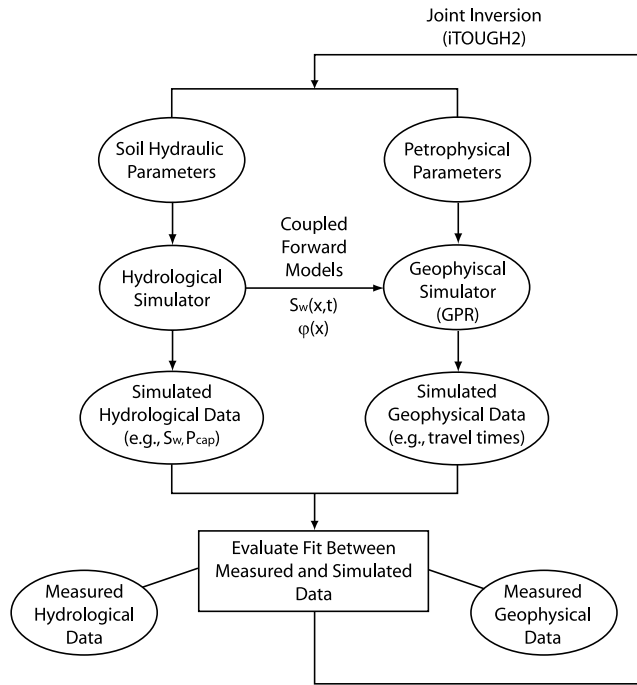
Figure 2. Flow chart for joint inversion of geophysical and hydrological measurements using framework of iTOUGH2 [*Finsterle*, 1999].

data. *Rucker and Ferré* [2004] used an analytical GPR ray-tracing model and an analytical unsaturated flow model to invert for the average hydraulic conductivity value with synthetic GPR cross-borehole travel time measurements collected through time at a single depth. They also demonstrated that two additional hydraulic parameters can be estimated if pressure head measurements are included in the inversion.

[8] Here we describe an approach for estimating soil hydraulic parameter distributions such as in the vadose zone through the coupled numerical simulation (and inversion) of multiple-offset cross-borehole GPR and hydrological data collected during transient flow experiments. Our approach uses GPR travel times directly and does not aim to obtain geophysical images (tomograms), avoiding some difficulties of cross-borehole tomography and allowing for a far less dense set of GPR data to be collected (thus allowing data sets to be collected in less time). While the methodology can be applied to any type of hydrological data, we focus on neutron probe measurements, which provide near-borehole estimates of water content. Coupling between the hydrological and GPR simulators links the simulated water saturation distributions and the generated porosity distributions to the simulated GPR data (e.g., travel times), thus indirectly linking the geophysical data to the soil hydraulic parameters. Joint inversion proceeds by perturbing the soil hydraulic parameters—which alters the simulated hydrological and geophysical data—until the simulated and measured hydrological and geophysical data are in good agreement. A flow chart depicting the joint inversion procedure, which we implemented in iTOUGH2

[*Finsterle*, 1999], is given in Figure 2, and details of the inversion methodology are discussed below.

[9] The methodology we employ is an extension of the work by *Kowalsky et al.* [2004a], which involved the joint use of geophysical and hydrological data within a maximum a posteriori (MAP) inversion framework [*McLaughlin and Townley*, 1996] that employed concepts from the pilot point method [*RamaRao et al.*, 1995; *Gomez-Hernandez et al.*, 1997]. The approach of *Kowalsky et al.* [2004a] allowed for estimation of unknown log-permeability values, at so-called pilot point locations, and other hydrological parameters, resulting in hydrological models that honored geophysical and hydrological data and that contained permeability distributions with specified patterns of spatial correlation and that honored available log-permeability point measurements. The method was shown to be useful for accurately predicting flow phenomena and quantifying parameter uncertainty. However, the forward model used to simulate GPR data was limited to a simple data acquisition configuration, disallowing the use of multiple-offset GPR measurements (discussed below) and generalized three-dimensional models. In addition, the petrophysical function was assumed to be known and error free, despite the fact that inaccuracies easily enter into the field-scale petrophysical function when it is derived using non-site-specific data or laboratory-scale measurements [e.g., *Moysey and Knight*, 2004; *Lesmes and Friedman*, 2005].

[10] At present the aforementioned method of *Kowalsky et al.* [2004a] is extended to allow for (1) inclusion of GPR measurements (travel times) collected using any transmitter and receiver geometry within a possibly three-dimensional model, and (2) estimation of petrophysical parameters. (We have also extended the method to allow for possible estimation of spatial correlation parameters, but this possibility is not currently explored herein.) These extensions permit investigations under more realistic conditions (e.g., where there is uncertainty in the petrophysical function) and increase the flexibility of GPR data acquisition configurations that may be considered, which allows for soil hydraulic parameter estimates with increased resolution and accuracy. Following a description of the methodology, given in section 2, synthetic examples and an application using field data are presented in sections 3 and 4, respectively.

2. Methodology

2.1. Hydrological Measurements

[11] The hydrological process considered in this study is variably saturated flow in the vadose zone. Variably saturated flow of incompressible water in non-deformable porous media can be modeled with the Richards' equation:

$$\varphi \frac{\partial S_w}{\partial t} + \nabla \left[\frac{K(S_w)}{\rho_w g} \nabla P^c(S_w) - K(S_w)\mathbf{z} \right] = 0, \qquad (2)$$

where K and P^c, both functions of water saturation S_w, are the unsaturated hydraulic conductivity and the capillary pressure, respectively, ρ_w is the water density, g is the gravitational constant, φ is the porosity, and $\mathbf{z}$ is the

vertically oriented unit vector (positive upward). The hydraulic conductivity is defined as:

$$K = k \frac{k_{rel}(S_w)\rho_w g}{\mu_w}, \qquad (3)$$

where k_{rel} is the dimensionless relative permeability (the only component of K that is a function of water saturation), μ_w is the dynamic viscosity of water, and k is the absolute permeability, which is a scalar k for the case of isotropic media, and which has horizontal and vertical components k_h and k_v, respectively, for the case of anisotropic media. For this study, we model the relative permeability and capillary pressure with the functions given by *van Genuchten* [1980] as:

$$k_{rel} = \sqrt{S}\left[1 - \left(1 - S^{m^{-1}}\right)^m\right]^2 \qquad (4)$$

$$P^c = -\alpha^{-1}\left(S^{m^{-1}} - 1\right)^{1-m} \qquad (5)$$

$$S = \frac{S_w - S_w^{res}}{S_w^{sat} - S_w^{res}}, \qquad (6)$$

where S is the normalized water saturation, and S_w^{res} and S_w^{sat} are the soil-specific residual and maximum water saturation values, respectively, and m (dimensionless) and α (Pa^{-1}) are soil-specific parameters. Hysteresis of the relative permeability function can affect the redistribution of water following infiltration [*Philip*, 1991], but is not considered in this study.

[12] To simulate flow in the vadose zone using equations (2)–(6), the soil hydraulic parameters φ, α, m, S_w^{res}, S_w^{sat}, and k must be specified. Although a number of studies suggest that spatial variability of these parameters can be significant, data describing such variability for modeling applications are limited [*Jury et al.*, 1987; *Russo and Bouton*, 1992]. The absolute permeability is commonly the parameter to which flow in the vadose zone is most sensitive, arguably making its characterization of primary importance. In the present work, all parameters are considered spatially uniform, except for k, which can be treated as a space random function (SRF).

[13] The joint inversion approach described below aims to estimate soil hydraulic parameters using a combination of hydrological measurements (e.g., water content values inferred from neutron probe logging) and ground-penetrating radar measurements (e.g., cross-borehole travel times), which are highly sensitive to the time- and space-varying distribution of S_w, which is in turn affected by the soil hydraulic parameters. The framework used for the coupled simulation (and inversion) of hydrological and geophysical data (discussed next) is iTOUGH2 [*Finsterle*, 1999], a code that provides parameter estimation capabilities for the TOUGH2 flow simulator [*Pruess et al.*, 1999].

2.2. Ground-Penetrating Radar Measurements

2.2.1. Petrophysical Function Relating Water Saturation and Porosity to Dielectric Constant

[14] Application of GPR measurements in the subsurface requires a petrophysical function that relates the soil water saturation and porosity to the dielectric constant (e.g., reviews are given by *Huisman et al.* [2003] and *Lesmes and Friedman* [2005]). One of the most commonly used models, by *Topp et al.* [1980], is given as a third-order polynomial:

$$\kappa = 3.03 + 9.3\theta + 146.0\theta^2 - 76.7\theta^3, \qquad (7)$$

where θ is the water content (the product of water saturation and porosity), and where the coefficients were determined through laboratory measurements on several inorganic soils. However, the dielectric constant of soils is sensitive to additional soil properties, such as the mineral composition of the solid soil particles [*Roth et al.*, 1990], organic matter and bulk density [*Jacobsen and Schjonning*, 1993], temperature [*Roth et al.*, 1990; *Or and Wraith*, 1999], and grain geometry and cementation [*Lesmes and Friedman*, 2005], all of which suggest the need for alternative petrophysical relationships that allow for site-specific variations.

[15] Alternatively, there are theoretically based models [*Lesmes and Friedman*, 2005], such as volumetric mixing formulae, which account for the volume fraction and geometrical arrangement of materials with known or measurable dielectric constants. An expression used for two-phase mixtures [*Birchak et al.*, 1974] and extended to three-phase mixtures of air, water, and solids [*Alharthi and Lange*, 1987; *Roth et al.*, 1990] is given by

$$\kappa = \left[(1 - \varphi)\kappa_s^n + S_w\varphi\kappa_w^n + (1 - S_w)\varphi\kappa_a^n\right]^{\frac{1}{n}}, \qquad (8)$$

where φ is the porosity, κ_s is the dielectric constant for the solid components, κ_w and κ_a are the known dielectric constants for water and air, respectively, and n is a parameter related to the geometric arrangement of materials relative to the applied electric field [*Ansoult et al.*, 1984]. The value of n is commonly assumed to be 0.5, which is expected in isotropic media [*Birchak et al.*, 1974], but measured values for sediments have been observed to range between 0.4 and 0.65 [*Chan and Knight*, 1999].

[16] The petrophysical model of equation (8) can be adjusted to site-specific conditions, given estimates of κ_s and φ. The measurement of porosity from cores can be problematic, since the in-situ packing of unconsolidated or semi-consolidated materials is difficult to preserve through the coring process. Values of κ_s are sometimes assumed (e.g., a "representative" value is taken from the literature) or are determined with cores in the laboratory using time-domain reflectometry (TDR) methods [*Topp et al.*, 1980; *Martinez and Byrnes*, 2001]. However, errors can be unintentionally introduced from several sources during this process. As petrophysical functions are frequency dependent [*Robinson et al.*, 2003, 2005], relationships derived in the laboratory from TDR measurements, for example, are not necessarily appropriate for application at the field scale [*Huisman et al.*, 2003; *Moysey and Knight*, 2004], where the frequencies employed are typically lower than in the laboratory. Petrophysical functions may also be derived in the field by correlating dielectric constant estimates, derived from cross-borehole GPR, with estimates of water content inferred from co-located neutron probe (NP) data [*Hubbard

et al., 1997]. However, tomogram artifacts (such as those resulting from smoothing, noisy data, or smearing due to limited ray coverage [*Stewart*, 1991]) and errors in NP data [*Yao et al.*, 2004; *Fares et al.*, 2004] can introduce errors into the estimated petrophysical function [*Huisman et al.*, 2003; *Day-Lewis and Lane*, 2004; *Moysey et al.*, 2005; N. Linde et al., Inversion of tracer test data using tomographic constraints, submitted to *Water Resources Research*, 2005].

[17] As will be described in section 2.3, our inversion approach allows for the estimation of petrophysical parameters in equation (8)—at present, we consider the estimation of κ_s—thus helping to overcome potential errors introduced by scale discrepancy and measurement error. It should be noted that we currently assume the error in the petrophysical function is contained entirely in the parameters, not in the petrophysical model itself; the flexible form of equation (8) ensures that it can be applied in most real-world situations.

2.2.2. Simulation of GPR Data

[18] Numerous techniques are available for simulating GPR data, ranging from ray-based methods [*Cai and McMechan*, 1995; *Sethian and Popovici*, 1999], to pseudo-spectral methods [*Casper and Kung*, 1996], to time-domain finite-difference full-waveform methods [*Kunz and Luebbers*, 1993; *Bergmann et al.*, 1998; *Kowalsky et al.*, 2001]. Ray-based methods are the simplest and most computationally efficient for the simulation of GPR travel times; they are based on a high frequency approximation that calculates the arrival time of the first break of the transmitted wave (i.e., the time at which the wave amplitude departs from zero) and ignores the remainder of the waveform [*Bregman et al.*, 1989]. While a full-waveform finite-difference method is used in the synthetic examples of this study to simulate GPR data, the straight-ray method is used for inversion; we examine whether the straight-ray approximation, chosen for computational efficiency, significantly impacts the estimated parameters and predicted system behavior. As will be discussed in the synthetic examples given below, significant errors can arise in travel times simulated using the straight-ray method, depending on the corresponding water distribution, leading in some cases to a systematic error (over-prediction) in simulated travel times that must be accounted for in the inversion procedure.

[19] The travel time T for an EM wave traveling between the transmitting and receiving antennas in a domain characterized by discrete grid blocks can be approximated by defining a straight ray between the antennas and summing the travel times through each grid block that the ray travels:

$$T = \sum_{i=1}^{N} \frac{L_i}{V_i}, \qquad (9)$$

where L_i is the length of the travel path (linear line segment) in block i, N is the number of blocks through which the ray passes, and V_i is the EM velocity in block i. For the present work, the petrophysical function is modeled using the volumetric mixing formula of equation (8), which, through combination with equations (1)

and (9), allows for the travel time T to be calculated as follows:

$$T = \sum_{i=1}^{N} \frac{L_i}{c} \left[(1 - \varphi_i)(\kappa_s)^n + S_{w,i}\varphi_i(\kappa_w)^n + (1 - S_{w,i})\varphi_i(\kappa_a)^n \right], \qquad (10)$$

where $S_{w,i}$ and φ_i are the water saturation and porosity in grid block i, respectively. Since porosity is presently assumed to be constant $\varphi_i = \varphi$.

[20] While more sophisticated methods (such as curved-ray methods) are reasonable alternatives for use in joint inversion, they would be computationally demanding, especially for three-dimensional models. Note that our methodology involves large numbers of parameter perturbations, each of which requires an entire flow simulation and a full set of simulated GPR surveys. Furthermore, curved-ray paths would need to be calculated for all antenna combinations that are used for each survey and for each parameter perturbation. Application of curved-ray methods to models with irregular grids would pose additional difficulties.

[21] The straight-ray travel time approximation (see equation (10)) allows for most calculations to be done only once and before the inversion begins (e.g., the list of values L_i for each combination of transmitting and receiving antennas). Additionally, irregular and three-dimensional models are easily and efficiently simulated. The appropriateness of the straight-ray approximation is further discussed in section 3.1.1.

[22] In this work, the simulation of cross-borehole GPR travel times in a domain undergoing transient fluid flow was made possible through solution of equation (10) within iTOUGH2 [*Finsterle*, 1999]. Each travel time is thus a function of the distributions of water saturation and porosity, the variable dielectric parameters (n, κ_s), and remaining known parameters.

2.3. Joint Inversion Methodology

[23] Here we extend the method developed by *Kowalsky et al.* [2004a] for estimating flow parameter distributions in the vadose zone using hydrological and geophysical data collected during transient flow experiments. The approach used a maximum a posteriori (MAP) inversion framework [*McLaughlin and Townley*, 1996; *Rubin*, 2003] and employed concepts from the pilot point method [*RamaRao et al.*, 1995; *Gomez-Hernandez et al.*, 1997]. Application of pilot point methods involves the generation of spatially correlated parameter fields, which are subsequently perturbed by changing the values at select conditioning points (referred to as pilot points) to minimize the misfit between measured and simulated data (which could include both hydrological and geophysical data).

[24] At present, the permeability distribution is anisotropic and treated as a lognormal SRF. The spatially varying component of permeability is introduced through the permeability modifier $\xi(x)$, defined through the following relationships:

$$k_v(\mathbf{x}) = k_v 10^{\xi(x)} \qquad (11)$$

$$k_h(\mathbf{x}) = k_h 10^{\xi(x)} \qquad (12)$$

where k_v and k_h are the mean values of vertical and horizontal permeability, respectively, and $\xi(\mathbf{x})$ is an SRF with known patterns of spatial correlation (i.e., known semivariograms). Given the frequent availability of semivariograms derived from well data and investigations of nearby outcrops or sites with similar geology, it is considered reasonable to assume that the spatial correlation patterns are known. However, we note again that the methodology does not prevent the spatial correlation parameters from being treated as unknowns. The mean of $\xi(\mathbf{x})$ is zero and its variance is equivalent, as is the semivariogram, to that of the log distributions of $k_h(\mathbf{x})$ and $k_v(\mathbf{x})$.

[25] The permeability modifier field is parameterized using pilot points, giving a vector of unknowns (ξ_{pp}) at the pilot point locations. Through sequential simulation [*Deutsch and Journel*, 1992], a permeability modifier field conditional to ξ_{pp} is generated. During the inversion procedure, the vector ξ_{pp} is repeatedly perturbed as $\xi(\mathbf{x})$ is updated through sequential simulation, until the log-permeability field (calculated with equations (11) and (12)) is found that provides (1) an optimal match to the observed hydrological and geophysical data, and (2) minimal deviation of the unknowns from prior estimates, if available. The remaining unknown model parameters are simultaneously estimated with ξ_{pp}.

[26] In previous work, the petrophysical function was assumed to be known and error free. In addition, the technique used for simulating ground-penetrating radar measurements was limited to one simple data acquisition configuration, the zero-offset profile (ZOP), in which the transmitting and receiving antennae are kept at equal depths during each measurement. This acquisition geometry yields a single depth profile of GPR travel times. While ZOP surveys are useful for gaining depth-averaged information, they cannot be used to resolve lateral variations in material properties.

[27] Presently our methodology incorporates equation (10) for the calculation of GPR travel times for any transmitter and receiver combination (i.e., multiple-offset profile surveys). We accommodate two- and three-dimensional models with grid cells of any shape (regularly-spaced grids are not required). Additionally, we expand the parameters that can be considered as unknowns to include the vector of soil hydraulic parameters, such as $\mathbf{a_h} = [\varphi, \alpha, m, S_w^{res}, S_w^{sat}, k_h, k_v, \ldots]$ from equations (2)–(6); the vector of petrophysical parameters $\mathbf{a_\kappa} = [\kappa_s, n]$ from equation (8); and, while not explored in this study, semivariogram parameters, including, for example, the range parameter occurring in most semivariogram models [*Deutsch and Journel*, 1992]. These extensions permit investigations under more realistic conditions, such as where there is uncertainty in the petrophysical function as well as in the spatial correlation function. Moreover, as opposed to the ZOP surveys previously considered, the wealth of data available in multiple-offset profile surveys improves the accuracy and resolution of estimated soil hydraulic parameters.

[28] The general goal of the inverse problem in this study is the estimation of vectors $\mathbf{a} = [\mathbf{a_h}, \mathbf{a_\kappa}]$ and ξ_{pp} given the following measurements:

[29] 1. GPR travel time measurements (T), given as $\mathbf{z}_{GPR} = T(\mathbf{x}_{Tx}^t, \mathbf{x}_{Rx}^t) + \mathbf{e}_{GPR}$, for survey times $\mathbf{t}$ (length n) and

taken for the transmitting and receiving antenna positions $\mathbf{x}_{Tx}^t$ and $\mathbf{x}_{Rx}^t$, such that

$$
\begin{aligned}
\left(\mathbf{x}_{Tx}^t, \mathbf{x}_{Rx}^t\right) = &\left(x_{Tx(1)}^{t_1}, x_{Rx\left(k=1, M_{1,1}\right)}^{t_1}\right), \\
&\left(x_{Tx(2)}^{t_1}, x_{Rx\left(k=1, M_{1,2}\right)}^{t_1}\right), \\
&\quad\quad\quad \vdots \\
&\left(x_{Tx(N_1)}^{t_1}, x_{Rx\left(k=1, M_{1,N_1}\right)}^{t_1}\right), \\
&\left(x_{Tx(1)}^{t_2}, x_{Rx\left(k=1, M_{2,1}\right)}^{t_2}\right), \\
&\left(x_{Tx(2)}^{t_2}, x_{Rx\left(k=1, M_{2,2}\right)}^{t_2}\right), \\
&\quad\quad\quad \vdots \\
&\left(x_{Tx(N_2)}^{t_2}, x_{Rx\left(k=1, M_{2,N_2}\right)}^{t_2}\right), \\
&\left(x_{Tx(1)}^{t_n}, x_{Rx\left(k=1, M_{n,1}\right)}^{t_n}\right), \\
&\left(x_{Tx(2)}^{t_n}, x_{Rx\left(k=1, M_{n,2}\right)}^{t_n}\right), \\
&\quad\quad\quad \vdots \\
&\left(x_{Tx(N_n)}^{t_n}, x_{Rx\left(k=1, M_{n,N_n}\right)}^{t_n}\right)
\end{aligned}
$$

where $M_{i,j}$ is the number of receiving antenna positions for transmitting antenna $x_{Tx(j)}^{t_i}$ at survey time t_i. The length of the vectors $\mathbf{x}_{Tx}^t$ and $\mathbf{x}_{Rx}^t$ depends on the number of transmitting and receiving antenna combinations used for each survey time, and is given by $\sum_{i=1}^{n}\sum_{j=1}^{N_i} M_{i,j}$. The measurement error vector associated with measurement of $\mathbf{z}_{GPR}$ is of the same length and is given by $\mathbf{e}_{GPR}$. This general notation allows for data to be collected for varying subsets of receiving and transmitting antenna positions at different times.

[30] 2. Hydrological measurements, given here as local water content measurements (e.g., inferred from NP data) $\mathbf{z}_H = \varphi \cdot S_w[(\mathbf{x}_H^{t_H})] + \mathbf{e}_H$, taken at borehole positions $\mathbf{x}_H$ (length M_H) and at survey times $\mathbf{t}_H$ (length n_H), where $\mathbf{e}_H$ is the measurement error associated with measurement of $\mathbf{z}_H$ (length $M_H \times n_H$). As noted previously, the porosity is assumed to be spatially uniform in the examples given below, although the methodology does not require it.

[31] Accurate characterization of $\mathbf{e}_{GPR}$ is significant but challenging, since its magnitude and distribution depend on antenna separation distance and vertical offset. We hypothesize that accounting for spatial variations in $\mathbf{e}_{GPR}$ is of secondary importance for the current application due to spatial averaging effects and data redundancy (overlapping of ray paths traveling between different antenna positions). For simplicity we model the distribution of $\mathbf{e}_{GPR}$ as independent of time and antenna position and leave related investigations for future research.

[32] In order to test the approach with minimal data requirements, we do not work with point measurements of
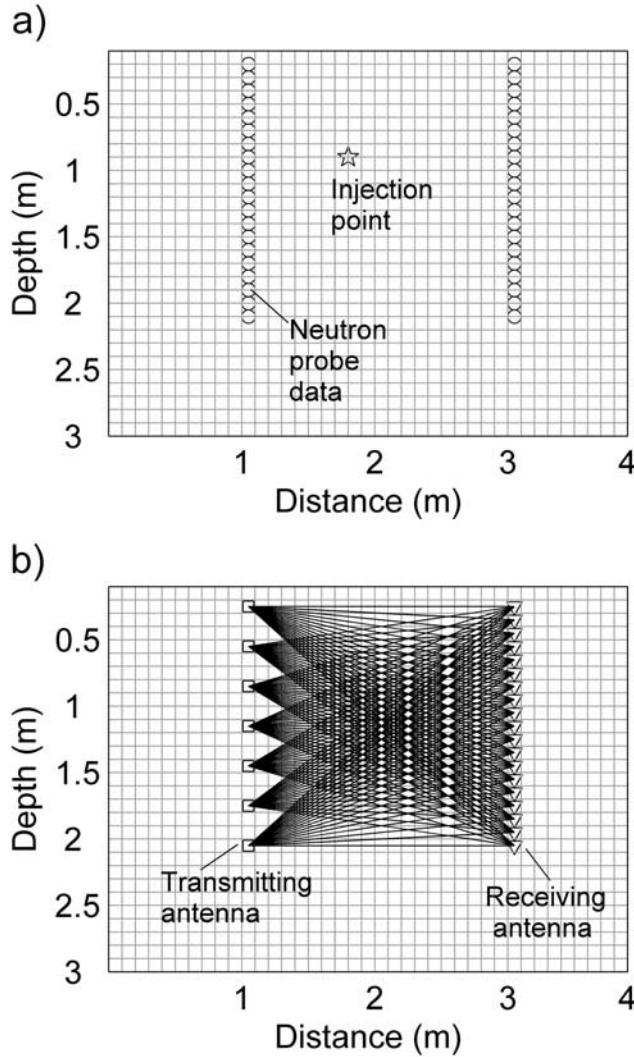
Figure 3. Model geometry for synthetic examples: (a) injection point and neutron probe measurement locations; (b) GPR antenna locations and the straight-ray paths used for inversion.

permeability in this study, although they can easily be included if they are available [*Kowalsky et al.*, 2004a]. As mentioned above, the geostatistical information describing the log-permeability SRF is assumed known from outcrop studies or previously characterized sites with similar geology [cf. *Rubin*, 2003] (section 2.3).

[33] Assuming that (a) the measurement error vectors $\mathbf{e}_{GPR}$ and $\mathbf{e}_H$ are characterized by known normal distributions, (b) the log-permeability field is uncorrelated with other soil-hydraulic parameters, and (c) the prior information of the parameters is normally distributed, then the objective function (OF) that is minimized during inversion can be written as:

$$OF(\mathbf{a}) = [\mathbf{z} - F(\mathbf{a})]^T \mathbf{C}_v^{-1} [\mathbf{z} - F(\mathbf{a})] + [\xi_{pp} - \bar{\xi}_{pp}]^T \mathbf{C}_{\xi_{pp}}^{-1} [\xi_{pp} - \bar{\xi}_{pp}] + [\mathbf{a} - \bar{\mathbf{a}}]^T \mathbf{C}_a^{-1} [\mathbf{a} - \bar{\mathbf{a}}],$$

(13)

where $\bar{\xi}_{pp}$ and $\bar{\mathbf{a}}$ are the prior means of ξ_{pp} and $\mathbf{a}$, respectively, and $\mathbf{C}_{\xi_{pp}}$ and $\mathbf{C}_a$ are the corresponding

covariance matrices. The variances of $\bar{\mathbf{a}}$ form the diagonal terms in $\mathbf{C}_a$ (the remaining terms are zero). For the case in which log-permeability point measurements are available, $\bar{\xi}_{pp}$ and its variance values (which are used as the diagonal terms in $\mathbf{C}_{\xi_{pp}}$) are calculated through kriging [*Deutsch and Journel*, 1992]. Since we currently assume that no log-permeability point measurements are available, the prior values of $\bar{\xi}_{pp}$ equal zero (i.e., each pilot point is penalized equally for deviating from the mean log-permeability value, which is one of the unknowns in $\mathbf{a}_H$); in addition, the diagonal values of $\mathbf{C}_{\xi_{pp}}$ contain the known log-permeability variance, ensuring that the log-permeability values at the pilot point locations stay reasonably close to the mean value $\mathbf{k}$.

[34] For models with spatially uniform soil properties (as in the example given in section 3.1), only one inversion realization is performed, giving MAP estimates that are equivalent to the weighed least squares solution. In models with heterogeneous permeability (as in the example given in section 3.2 and the application to field data given in section 4), multiple inversions are performed, each giving one realization of the MAP solution, and each obtained using a different initial log-permeability field (i.e., a seed number that is unique to each inversion realization is used for sequential simulation [*Deutsch and Journel*, 1992]).

[35] In the following examples, the Levenberg-Marquardt algorithm [*Levenberg*, 1944; *Marquardt*, 1963] was used to minimize the objective function.

3. Synthetic Examples

[36] The joint inversion methodology is demonstrated in this section using synthetic data collected during simulated water injections in the subsurface. The objective function of equation (13) can be used to estimate all unknowns or some subset of unknowns, depending on the problem being considered. Here we test the effectiveness of the method for estimating various subsets of unknowns (including permeability, anisotropy ratio, parameters of the capillary pressure and relative permeability functions, porosity, as well as a parameter from the petrophysical function) for two different heterogeneity conditions. In the first example (section 3.1), we consider a model with spatially uniform soil parameters. In the second example (section 3.2), we consider a model with a heterogeneous permeability distribution.

3.1. Model With Uniform Soil Hydraulic Parameters

[37] The model considered in the first example (Figure 3) has horizontal and vertical dimensions of 3 m and 4 m, respectively, grid spacing of 10 cm (in both directions), and spatially uniform soil hydraulic properties (Table 1). Boundary conditions are as follows: the total flux across the upper boundary, which represents the ground surface, is known; the lower boundary is fully saturated, representing the water table; and no-flow conditions are implemented at the vertical sides of the model. Because the steady-state water profile and the transient response to water injection depend on the hydraulic parameters, the simulation proceeds in two steps. First, the steady-state profile (gravity-capillary equilibrium) is simulated for the given set of hydraulic param-

Table 1. Properties Used for Synthetic Examples

Description	Parameter Values	
Hydrological parameters[a]	$\mu_w = 1.002 \times 10^{-3}$ Pa s, $\rho_w = 1000$ kg/m^3	
	$k_v = 5.0 \times 10^{-12}$ m^2, $k_h = 2.0 \times 10^{-11}$ m^2	
	$m = 2.69$, $\alpha = 3.573 \times 10^{-4}$ Pa^{-1}	
	$S_w^{res} = 0.083$, $S_w^{sat} = 1.0$	
	$\varphi = 0.364$	
Geostatistical model for log-permeability (spherical semivariogram)[b]	*Horizontal*	*Vertical*
$\gamma_k(h) = c_0 + c_1 [3/2(h/r) - 1/2(h/r)^3]$ (for h < r)	$c_0 = 0.01$	$c_0 = 0.01$
$\gamma_k(h) = c_0 + c_1$ (for h > r)	$c_1 = 0.5$	$c_1 = 0.5$
	$r = 6.0$ m	$r = 0.3$ m
Dielectric constant function[c]	$\kappa_s = 4.5$, $n = 0.5$	
Electrical conductivity function[d]	$a = 0.88$, $n* = 2.0$, $m* = 1.37$, $\sigma_w = 0.4$ mS/cm	
$\sigma = \sigma_w S_w^{n*} \varphi^{m*}/a$		

[a]Parameters defined in text; see description of (2)–(5).

[b]For example in section 3.2. *h* is separation distance (m), c_0 and c_1 are nugget and variance, respectively. The range is a measure of spatial persistence for the spherical semivariogram [*Deutsch and Journel*, 1992].

[c]Parameters defined in text; see description of equation (8).

[d]*Archie* [1942]; also see *Kowalsky et al.* [2004b] for description. Used for generating synthetic waveforms with finite difference method; not used in calculating straight ray travel times with (10).

eters. Second, using the steady-state profile to specify initial conditions, water injection and subsequent redistribution are simulated by imposing a mass flux of water equal to 1.08 kg/hr at the injection point for 12 hours duration. See Table 1 for a list of parameters used in the simulation.

[38] To test the inversion methodology, we simulated GPR and NP data before water injection (pre-injection) and several times after water injection (18, 24, 36, and 48 hours post-injection) in boreholes at horizontal positions of 1 m and 3 m (Figure 3). The synthetic NP data were obtained by recording the water content values during the simulation at the sampling locations shown in Figure 3a, and then adding measurement noise (zero-mean random deviates with standard deviation of 0.01).

[39] In this example, the time that would be required to collect GPR measurements (7 transmitting antennas × 19 receiving antennas = 133 measurements, as shown in Figure 3b) in the field would take only 15% of the time that would be required for the cross-borehole tomography example shown in Figure 1 (which had 28 transmitting antennas × 28 receiving antennas = 784 measurements).

[40] To obtain the GPR data for the "true" model, a two-dimensional finite difference code was implemented based on the method of *Bergmann et al.* [1998] and used to generate synthetic GPR waveforms with a central source frequency of 250 MHz. Grid spacing of 2 cm was used for both the horizontal and vertical directions, and the time step of 0.075 ns was used. Parameters describing the electrical properties that are needed for simulation are also given in Table 1. (Note that the electrical conductivity must be specified for the finite difference approach and is also a function of water saturation; see *Kowalsky et al.* [2004b] for details. We chose an electrical conductivity function that assumes surface conduction, such as due to the presence of clays, is negligible.) The travel time data were obtained by picking the first-break arrival times from the synthetic waveforms and then adding measurement noise (zero-mean random deviates with standard deviation of 0.25 ns).

[41] For emphasis, we note again that the GPR travel times used as synthetic data for inversion were calculated from the simulated full waveforms, which reflect complex EM wave propagation effects, such as ray curving; that is, the synthetic travel time data were not generated using the straight-ray approximation. However, to simulate GPR travel times during inversion, the straight ray approximation is used. In some cases this approximation leads to systematic errors, which is discussed in section 3.1.1.

[42] The simulated water saturation profiles for two times (pre-injection and 18 hours after onset of injection) are shown in Figures 4a and 4b. In addition, the corresponding GPR waveforms recorded for one selected transmitting antenna are shown in Figures 4c and 4d along with the travel times that were picked from the waveforms. Note the longer travel times resulting from the increased water saturation in the vicinity of the injection point.

3.1.1. GPR Travel Time Considerations

[43] For this uniform soil model (but not for the more realistic heterogeneous examples that follow), a systematic error (bias) in the simulated GPR straight-ray travel times occurs and must be accounted for to obtain good soil hydraulic parameter estimates. Figure 5 shows how error in the straight-ray travel times is related to the injection time and the distance that the straight-ray passes above or below the injection point (the errors were calculated relative to the travel times picked from waveforms simulated using the finite difference method, as discussed above). At early times, after the onset of injection but before the injected water spreads appreciably, the injected plume of water serves as a low velocity inclusion (increased water saturation results in decreased EM velocity) and causes a sharp contrast in the EM velocity. (For reference, at t = 18, 24, 36 and 48 hours, the maximum velocity decreases due to the inclusion are 20%, 17%, 14%, and 12%.) When the travel path of the earliest arriving energy is curved around the low-velocity inclusion, use of the straight-ray approximation
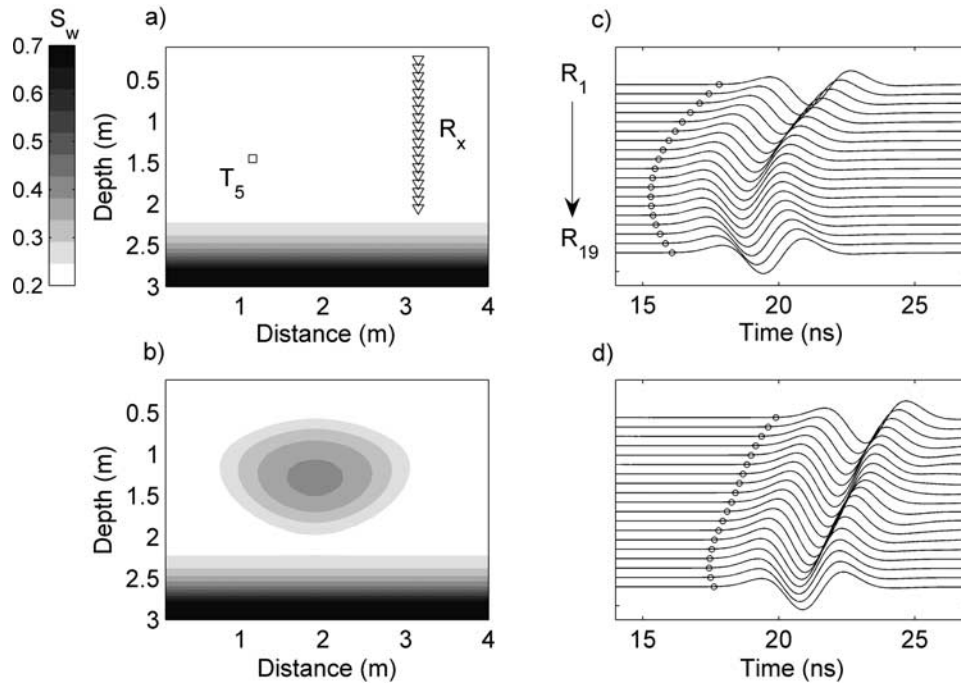
Figure 4. Simulated saturation profiles (a) before injection (steady state) and (b) 18 hours after onset of injection for model with uniform soil parameters. A single transmitting antenna position (T_5) is labeled with a square (there are 7 transmitting antenna positions in all, as shown in Figure 3), and the receiving antenna positions (R_x) are labeled with triangles. Simulated waveforms are shown in (c) and (d), corresponding to the simulation times for (a) and (b), respectively. Circles denote the arrival times (before measurement noise is added).

results in the inclusion appearing drier than it is in reality. While in this case the magnitude of the travel time error is small and on the order of the measurement noise (standard deviation of 0.25 ns), it is a systematic rather than random error and thus introduces a bias, which significantly affects the accuracy of the soil hydraulic parameter estimates obtained through inversion.

[44] The mean and standard deviation of the errors in the straight-ray arrival times for all post-injection surveys are 0.088 ns and 0.093 ns, respectively. (The corresponding values for the pre-injection survey are much lower: 0.014 ns and 0.011 ns.) To partially compensate for the bias in the GPR travel times simulated using the straight-ray approximation at early post-injection times, we include the post-injection shift in the arrival times (T_{shift}) as an unknown parameter to be estimated through inversion.

[45] The use of the relatively simple straight-ray approximation combined with the estimation of the T_{shift} parameter requires some justification. While more sophisticated forward models (such as curved-ray methods) are viable alternatives for use in joint inversion, they suffer from limitations of their own (discussed above), and they may include additional, uncertain parameters that need to be subjected to joint estimation to avoid a potential bias. Since estimation of only one additional parameter (T_{shift}) in the straight-ray model results in randomly distributed residuals and allows for accurate hydrological parameter estimates, the use of a more sophisticated model may not be warranted and may lead to overparameterization. Most importantly, we note again that estimation of the correction parameter is no longer necessary when dealing with more realistic hetero-

geneous models (as is discussed in the subsequent example in section 3.2).

3.1.2. Inversion Results

[46] Using the time-lapse GPR travel time and borehole NP measurements described above, we test the approach for two different sets of unknown parameters (refer to Table 2).
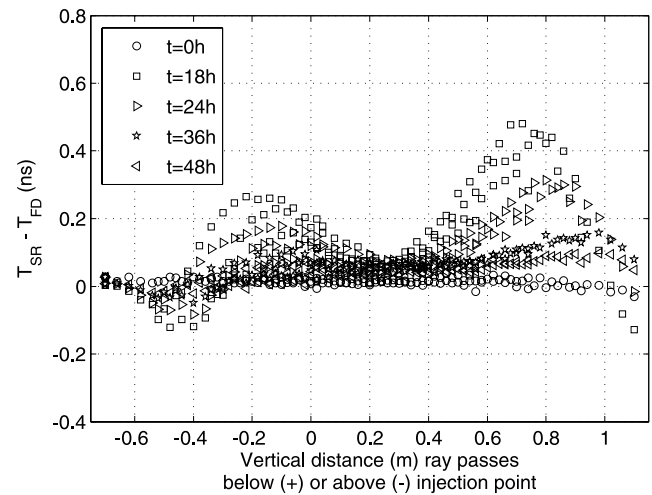

Figure 5. Difference between straight-ray travel times (T_{SR}) and the travel times calculated using a finite difference method (T_{FD}) versus vertical distance by which ray passes above or below injection point (for model with uniform soil parameters).

Table 2. Estimated Parameters for Synthetic Model With Uniform Soil Hydraulic Parameters[a]

	κ_s	$\log k_v$ [k_v, m^2]	k_v/k_h	m	$\log (1/\alpha)$ [α, Pa^{-1}]	φ	T_{shift}, ns
True model	4.5	−11.301	0.25	2.69	3.447	0.364	N/A
Case 1a	*fixed*	−11.270 (±0.022)	0.3230 (±0.3E-3)	*fixed*	*fixed*	0.384 (±0.006)	0.125 (±0.03)
1b	{5.4}	−10.679 (±0.019)	0.216 (±0.014)	*fixed*	*fixed*	0.467 (±0.005)	0.055 (±0.033)
1c	{3.6}	−12.243 (±0.056)	0.42 (±0.6E-3)	*fixed*	*fixed*	0.262 (±0.009)	0.26 (±0.04)
1d	4.52 (±0.046)	−11.262 (±0.043)	0.325 (±0.26E-3)	*fixed*	*fixed*	0.384 (±0.008)	0.119 (±0.033)
Case 2a	*fixed*	−11.2308 (±0.051)	0.252 (±0.007)	2.57 (±0.063)	3.38 (±0.04)	*Fixed*	0.0916 (±0.034)
2b	{5.4}	−11.550 (±0.046)	0.167 (±0.014)	4.495 (±0.261)	3.77 (±0.04)	*Fixed*	−0.0216 (±0.038)
2c	{3.6}	−11.225 (±0.048)	0.570 (±0.047)	2.160 (±0.033)	3.32 (±0.02)	*Fixed*	0.199 (±0.04)
2d	4.496 (±0.042)	−11.176 (±0.025)	0.223 (±0.023)	2.480 (±0.003)	3.34 (±0.02)	*Fixed*	0.123 (±0.034)

[a]The word "*fixed*" indicates that the true parameter value from the model is assumed to be known for that case; values in braces are the incorrect values used in inversion to test sensitivity to the error in κ_s; values in parentheses are the marginal standard deviations of the estimated parameter.

In Case 1, the vertical component of the log-permeability (k_v), the anisotropy ratio (k_v/k_h), the porosity (φ), and the parameter T_{shift} are estimated. In Case 2, two parameters of the relative permeability and capillary pressure functions, namely m and $\log 1/\alpha$, are estimated, along with the vertical component of the log-permeability, the anisotropy ratio, and the parameter T_{shift}. In addition, for both cases we investigate various scenarios of uncertainty in the petrophysical function: (a) the petrophysical function is known accurately; the assumed or measured solid component dielectric constant (κ_s) in the petrophysical function is inaccurate (i.e., it contains an error of (b) +20% and (c) −20%); and (d) the parameter κ_s is estimated through inversion along with the remaining unknown parameters. For this example, we assume no prior information is available for the unknown parameters (i.e., the prior pdfs are uniform), yielding the objective function (13) with only the first term.

[47] When the petrophysical parameters are known accurately, as in Case 1a, reasonably accurate estimates of the hydraulic parameters are obtained, although the anisotropy ratio is over-predicted (Table 2). The difference between the predicted water saturation distribution and that of the true model at a single time is depicted in Figure 6, showing good overall agreement (maximum relative difference of 10%) with a slight under-prediction of water saturation in the vicinity of the plume. The parameter T_{shift} is estimated to be 0.125 ns, which is similar to the expected average bias in the straight-ray approximation, as discussed above.

[48] In practice, a small (or large) amount of error can be unintentionally introduced into the petrophysical function, for example, when a petrophysical function derived from laboratory scale measurements is employed at the field scale, or when an unconfirmed generic function is used at a given site. To examine the impact of realistic errors in the petrophysical parameters on inversion results, we intentionally use incorrect values for the parameter κ_s (errors of ±20% of its true value of 4.5). The resulting errors in the hydraulic parameter estimates are substantially increased (Cases 1b and 1c in Table 2), most notably: the porosity is over-predicted and under-predicted by almost 30% for Cases 1b and 1c, respectively; and the anisotropy ratio is over-predicted by 60% for Case 1c. As shown in Figure 6, the water saturation profile is over-estimated (by up to 65%) and under-estimated (by up to 30%) for Cases 1b and 1c, respectively.

[49] Note that the petrophysical function (see equation (8)) depends not only on κ_s but also on porosity, which was estimated through inversion. The erroneous values of κ_s assumed for Cases 1b and 1c and the corresponding inaccurate porosity estimates lead to highly inaccurate petrophysical functions (Figure 7).

[50] Because errors in the petrophysical function can adversely affect hydraulic parameter estimates, our inversion methodology allows for such errors to be partially compensated by allowing one or more of the petrophysical parameters to be unknown ($\mathbf{a}_{GPR}$) and jointly estimated with the remaining soil hydraulic parameters ($\mathbf{a}_h$). For Case 1d, the parameter κ_s is considered unknown and is estimated along with the remaining soil hydraulic parameters, which are estimated more accurately than for the two previous cases (e.g., the error in the porosity estimate is reduced to 5%). Consequently, the saturation profile is better predicted, to similar accuracy as for the case in which the parameter κ_s was error free (Case 1a).

[51] In Cases 2a–2d we include in the estimation procedure two parameters of the capillary pressure and water retention functions—namely m and $\log 1/\alpha$—and we again consider several scenarios of uncertainty in the petrophysical function. Based on Table 2 (and Figure 6) the
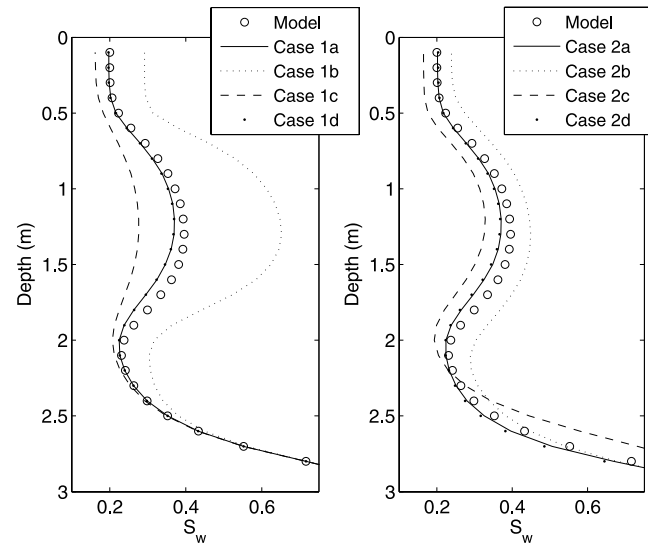

Figure 6. Predicted saturation profiles at 18 hours after onset of injection for Cases 1a–1d (left) and Cases 2a–2d (right) for example in section 3.1. The profiles are vertical slices taken from the two-dimensional models at a horizontal distance of 2 m.
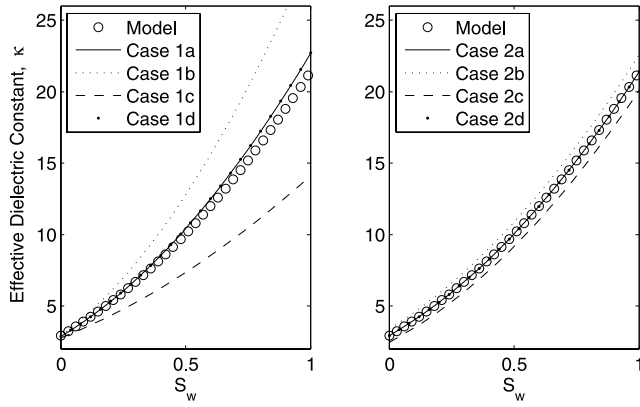
Figure 7. Petrophysical functions for Case 1 (left) and Case 2 (right) of example in section 3.1.

following observations can be made: (1) knowing the parameter κ_s accurately allows for reasonable estimates of the soil hydraulic parameters and good predictions of water saturation (Case 2a); (2) the presence of error in the petrophysical function adversely affects estimates of the soil hydraulic parameters and of the predicted water saturation profiles (Cases 2b and 2c); and (3) adverse effects of uncertainty in the parameter κ_s are minimized when κ_s is jointly estimated with the remaining hydraulic parameters (Case 2d).

[52] The capillary pressure and relative permeability functions obtained for Cases 1 and 2 are shown in Figure 8. The parameters of these functions were assumed to be known in Case 1, whereas two parameters were estimated in Case 2 (see Table 2).

[53] Note the low error in the estimated petrophysical parameters for Cases 2b and 2c, relative to those for Cases 1b and 1c; this is because in Case 2 the correct porosity value is assumed, leaving only inaccuracy in κ_s to affect the petrophysical function (Figure 7). However, as was shown above, small inaccuracies in κ_s were sufficient to cause large errors in the hydraulic parameter estimates, but joint estimation of κ_s allowed for such inaccuracies to be largely overcome.

3.2. Model With Heterogeneous Permeability

[54] The model explored in this example is identical to the one explored in section 3.1, except that now the log-permeability is spatially heterogeneous (Figure 9a), having been generated using sequential simulation [*Deutsch and Journel*, 1992] with an anisotropic spherical semivariogram (relevant parameters are given in Table 1). The remaining soil hydraulic parameters are modeled as spatially uniform. Synthetic data sets were obtained in the same fashion as in the previous example, except that the surveys for times of 12, 24, 36, and 48 hours after injection are used, in addition to the pre-injection survey. Measurement noise was added to the synthetic NP and GPR data sets in the same manner as for the previous example.

[55] Various studies have examined the placement of pilot points [*RamaRao et al.*, 1995; *Gomez-Hernandez et al.*, 1997], but most applications involved horizontal flow in the saturated zone. Currently, we use a configuration, tested by *Kowalsky et al.* [2004a] in an application similar to the present one, in which pilot points are placed on a regular grid. We estimate pilot point values along two vertical columns placed between the boreholes (see Figure 9a). The spacing in the vertical direction is finer than in the horizontal direction due to the shorter correlation length scale of heterogeneity in the vertical direction. Note that the computation time required for inversion increases with the number of pilot points (unknowns), which makes it necessary to balance the desired model resolution with computational limitations, especially for three-dimensional models (such as is considered in section 4). In the present example, 17 unknowns are estimated in total, namely, the
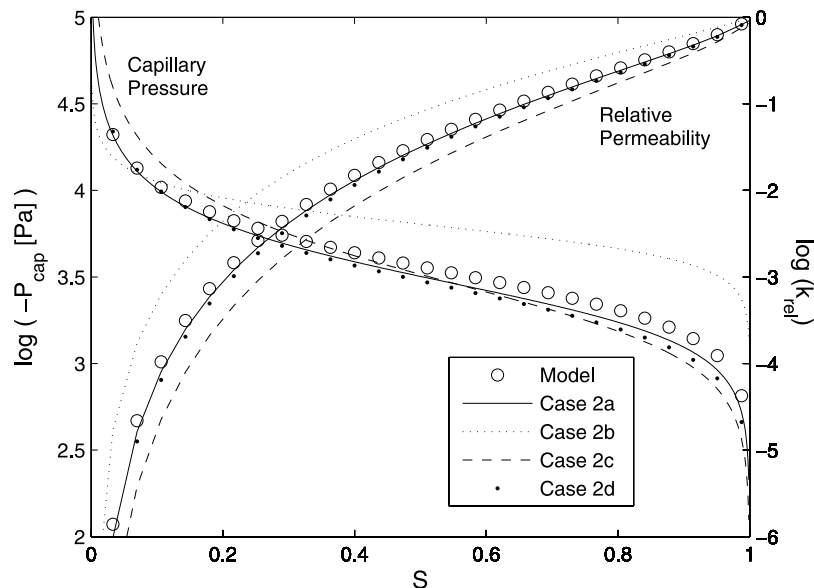

Figure 8. Capillary pressure function (left axis) and relative permeability function (right axis) for example in section 3.1. For Case 1, the relative permeability function and the capillary pressure function are fixed to those of the true model (circles). For Case 2, the parameters $\log(1/\alpha)$ and m of the capillary pressure function and relative permeability function are estimated through inversion.
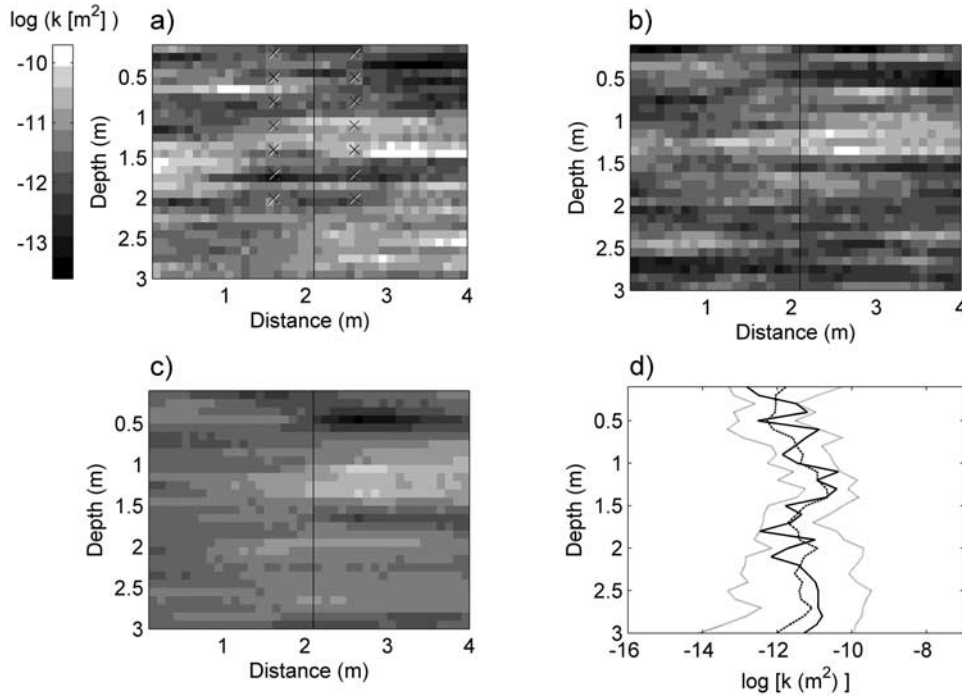
Figure 9. (a) True log-permeability distribution for model in section 3.2, (b) single realization of estimated permeability field, (c) the ensemble mean of the predicted distributions, and (d) vertical cross section showing distribution for true model (solid line), mean of the predicted distributions (dashed line), and the uncertainty bounds for predicted distributions (dotted lines), defined as ±2 standard deviations. The crosses in (a) indicate pilot point locations used for inversion.

uniform soil hydraulic parameters φ and log k_v, 14 pilot point permeability modifier values ξ_{pp}, and the petrophysical parameter κ_s.

[56] Recall that the entire permeability field is generated conditional to the permeability modifier values at the pilot point locations, such that estimating the optimal pilot point values is tantamount to determining the optimal permeability distribution of the entire model.

[57] The total flux at the surface is assumed to be known, as are the variance of the permeability field ($c_0 = 0.5$) and the parameters of the log-permeability semivariogram (the range r is 0.3 m in the vertical direction and 6.0 m in the horizontal), the permeability anisotropy ratio ($k_h = 4k_v$), and remaining soil hydraulic parameters (see Table 1). Note that the purpose of the examples presented here is not to design the optimal injection experiment, but rather to demonstrate the merit of the joint inversion approach.

3.2.1. GPR Travel Time Considerations

[58] In the previous example (section 3.1), which utilized a uniform soil model, it was necessary to account for systematic error in the travel times resulting from the straight-ray approximation. However, in the present example, which contains a heterogeneous permeability distribution, there is minimal systematic error in the simulated straight-ray travel times. Because the injected water is dispersed and distributed more heterogeneously, corresponding to an increased "randomness" in the EM velocity field (as compared to the elliptically shaped plume in the previous example), the actual ray paths no longer bend in a highly focused fashion around the injected water plume, making estimation of the parameter T_{shift} unnecessary. (For reference, at

t = 12, 24, 36 and 48 hours, the maximum velocity decreases due to the inclusion are 36%, 24%, 22.3%, and 22.1%, respectively.)

[59] For comparison with the previous synthetic example (for data simulated at 18 hours after onset of injection), the mean and standard deviation of the errors in the straight-ray arrival times for the post-injection surveys, relative to the travel times picked from waveforms simulated using the finite difference technique, are 0.055 ns and 0.20 ns, respectively. The corresponding values of the pre-injection survey are −0.020 ns and 0.043 ns.

3.2.2. Inversion Results

[60] Using the time-lapse GPR travel times and NP data simulated for the heterogeneous model, we test the approach for the case in which the soil hydraulic parameters and the petrophysical parameter κ_s are unknown, as described above. We assume no prior information is available for the unknown parameters, except for parameters of the log-permeability semivariogram function (including the variance), yielding the objective function with the first and second term (see equation (13)). We performed 20 inversion realizations, each with a different realization of the initial permeability field, resulting in 20 equally plausible sets of parameters. (Additional realizations were unnecessary in this case since the ensemble statistics of the estimates stabilized sufficiently.)

[61] The estimated log-permeability distributions compare well with that of the true model (as an example, one inversion realization is shown in Figure 9b). The mean of the multiple realizations is smooth, capturing the true model within the error bounds (see Figures 9c and 9d). Note that while the mean of the permeability realizations is smooth, the
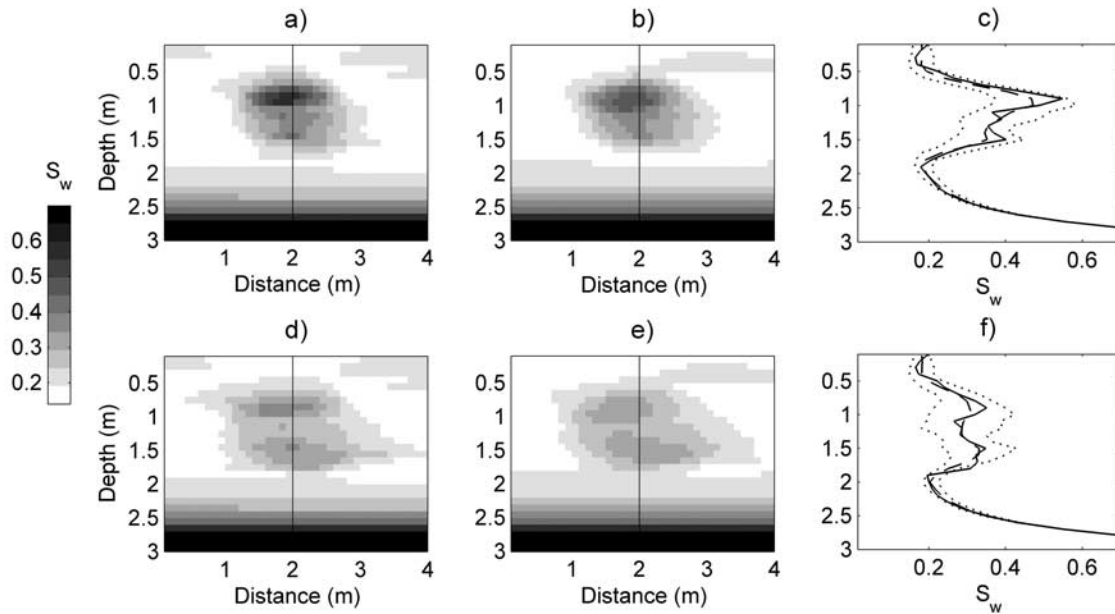
Figure 10. For heterogeneous model (section 3.2), (a) the distribution of water saturation in the true model, (b) the ensemble mean of the predicted water distributions, and (c) vertical cross section of water saturation for true model (solid line), the average of the predicted distribution of water saturation (dashed line), and the uncertainty bounds (dotted lines) at 12 hours after the onset of water injection. Plots similar to those in (a)–(c) are shown in (d)–(f) for the time of 24 hours after the onset of injection.

permeability fields estimated for each inversion realization reflect, on average, the specified spatial correlation model. Thus, the multiple permeability realizations could be used to predict flow phenomena, for example, the pdf of break-through time of the injected water reaching a control plane.

[62] The predicted water saturation profiles, on average, match that of the true model (Figure 10). The peaks in water saturation near 1 and 1.5 meters depth are slightly under-predicted, especially for the earlier time shown (12 hours after the onset of injection). However, in all cases the peaks fall within the uncertainty bounds of the predicted profiles (Figures 10c and 10f).

[63] The average of the predicted petrophyiscal functions, based on the estimated values of φ and κ_s, is nearly identical to that of the true model (Figure 11).

4. Application to Field Data From DOE Hanford Site

[64] An application of the joint inversion method to a field data set is given in this section. The purpose is not to develop an optimal hydrological model for the field site considered, but rather to demonstrate the method in the context of a three-dimensional setting with actual field data and to demonstrate the potential benefit that GPR measure-ments offer for estimating soil hydraulic parameters.

4.1. Description of Site and Experiment

[65] At the U.S. Department of Energy Hanford site, in Washington, vast quantities of highly radioactive waste and other toxic fluids have leaked into the vadose zone [e.g., *Sisson and Lu*, 1984; *Gee and Ward*, 2001; *Hunt and Gee*, 2002] and have necessitated the development of methods for monitoring and ultimately controlling the spread of contamination. Here we consider the Hanford 200 East Area

field site (also known as the "Sisson and Lu site"), which has been the subject of a number of experiments [*Sisson and Lu*, 1984; *Fayer et al.*, 1993, 1995; *Gee and Ward*, 2001], and for which laboratory investigations of soil properties have been reported [*Freeman et al.*, 2001; *Last and Caldwell*, 2001; *Last et al.*, 2001; *Schaap et al.*, 2003]
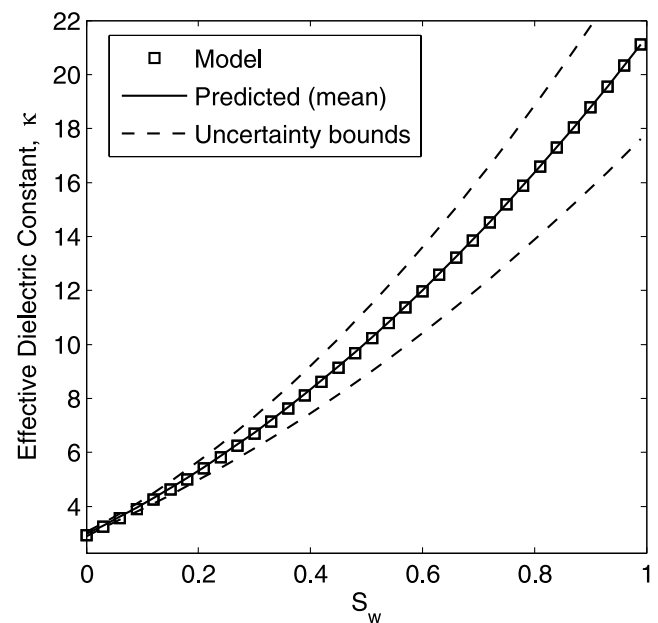

Figure 11. Petrophysical functions for heterogeneous example in section 3.2: true model (squares); ensemble mean of the estimated petrophysical functions (solid line); and uncertainty bounds (dashed lines), defined as ± two standard deviations.
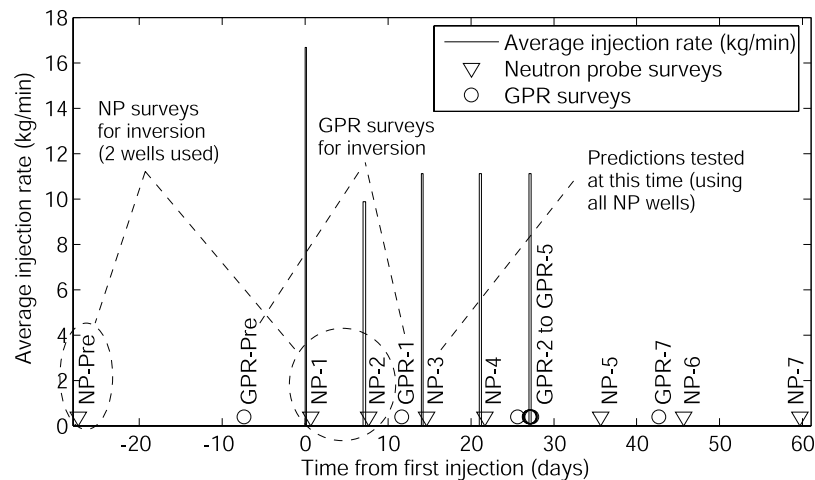
Figure 12. Measurement schedule for injection experiment at Hanford site. NP and GPR data sets were collected before the first injection (NP-pre and GPR-Pre, respectively) and at later times (NP-1 to NP-7, and GPR-1 to GPR-7, respectively). A limited subset of NP data were used for inversion (2 wells indicated in Figure 13 at survey times NP-Pre, NP-1, and NP-2). The GPR data sets used for inversion are GPR-Pre and GPR-1.

and modeling studies performed [*Smoot and Lu*, 1994; *Smoot and Williams*, 1996; *Rockhold et al.*, 1999; *Zhang et al.*, 2004].

[66] The infiltration experiment we consider began in May of 2000 and consisted of 5 injections of water over a period of one month. Each injection of approximately 4000 L of water lasted between 4 and 6.75 hours. During the experiment, extensive NP measurements [*Ward et al.*, 2000] and other geophysical data sets, including cross-borehole GPR [*Majer et al.*, 2000] and electrical resistance tomography (ERT) measurements [*Ramirez et al.*, 2001], were collected. The schedule for the injections and the surveys are depicted in Figure 12. Baseline surveys for both the GPR and NP measurements were collected before injection, and these are thought to reflect steady-state conditions. The NP surveys were typically conducted on the day following each injection, whereas the GPR surveys were collected sporadically.

[67] The locations of the measurement access wells are shown in Figure 13. The dense NP measurements, collected at a depth interval of 30.5 cm, allow for construction of three-dimensional data sets through interpolation [e.g., *Ward et al.*, 2000]. However, in this example, only the data collected in 2 wells (see Figure 13) and at three survey times (NP-Pre, NP-1, NP-2) are used for inversion, as are the GPR data for only two survey times (GPR-Pre and GPR-1). The dense NP data derived from all NP wells are only used to test the distributions that are predicted with the calibrated models at the time for which survey NP-3 was collected (corresponding to 15 days after the initial injection). Note that the remaining figures show water content rather than water saturation in order to allow for comparison with the NP-derived water content data, which do not allow for separation into water saturation and porosity; porosity is estimated in the inversion procedure.

[68] Figure 14a shows the distribution of water content derived from the dense NP data cube (for NP data collected in all 32 wells at one survey conducted 15 hours after the initial injection of water). The locations of the wells in which cross-borehole GPR measurements were collected

are indicated in Figure 14b, as are the straight-ray paths for the GPR measurements used in this example (representing a small fraction of the GPR measurements that were actually collected).

4.2. Model With Heterogeneous Permeability

[69] We focus on a subset of the study area. The nodes of the hydrological model are indicated in Figure 13. The model domain is approximately 12 m in both horizontal directions, and 14 m in depth. The grid spacing ranges between 0.5 and 1.25 m in the horizontal directions, and
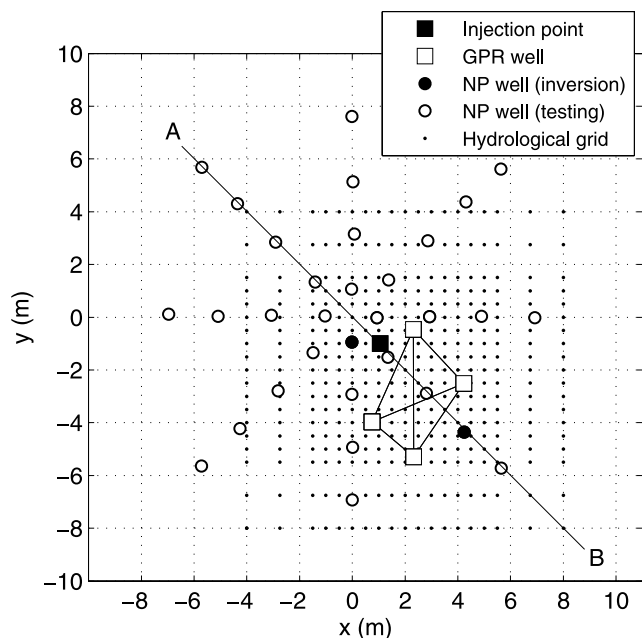

Figure 13. Measurement locations at the Hanford site and plan view of numerical grid used for hydrological modeling. Note that only 2 NP wells (solid circles) are used for inversion, while the remaining 30 NP wells (open circles) are only used to test the inversion results.
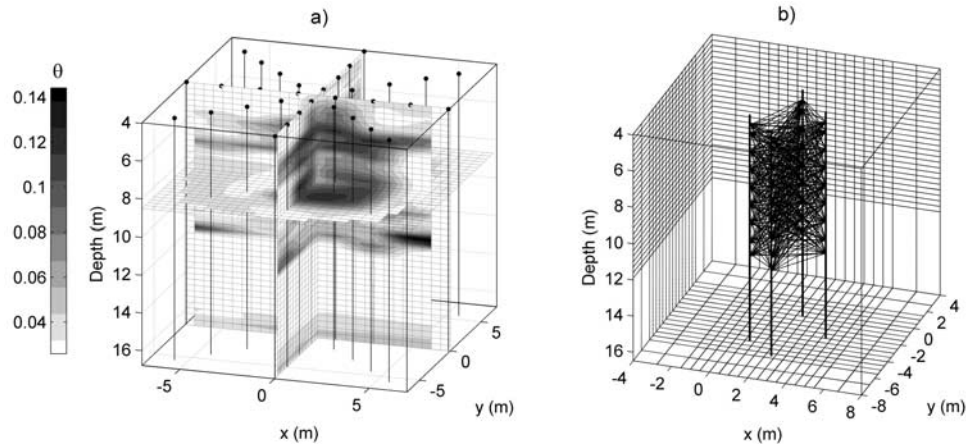
Figure 14. Available data sets collected during injection experiment at the Hanford site: (a) example of densely sampled NP data set (interpolated from NP wells, which are indicated by solid black vertical lines); (b) the straight-ray paths that are formed by the 4 GPR wells which are used for inversion.

equals 0.305 m in the vertical direction to allow for small-scale variability and to coincide with the vertical spacing of the NP measurements. The vertical grid spacing of the bottom layers is increased, since the water content in this region remains constant throughout the injection experiment. All elements in the top layer of the model are connected to one grid block, at which a small flux of water is applied to represent surface conditions. A free drainage boundary is implemented at the bottom of the model domain, as are no-flow boundaries at the four vertical sides. For the injection source, a time-dependent mass flow rate is specified at one grid point according to the schedule depicted in Figure 12. Since the actual time-varying flow rates are unknown (i.e., suspected to vary from the average values measured during the experiment), they are estimated with the remaining unknown parameters.

[70] Based on geostatistical analyses of permeability measurements, an anisotropic spherical semivariogram model was chosen to model the log-permeability. Various parameters that are either assumed or estimated in the present example are listed in Table 3.

[71] Using the two GPR travel time surveys (GPR-Pre and GPR-1) and a small subset of the available NP data (2 wells for surveys NP-Pre, NP-1, and NP-2), we test the

Table 3. Assigned and Estimated Parameters (Not Including Pilot Point Log-Permeability Modifier Estimates) for Application of Method to Hanford Field Data

Description	Fixed Parameter Values	Estimated Parameters (NP Data Only)	Estimated Parameters (GPR + NP Data)
Petrophysical function parameters. See equation (8).	$n = 0.5$	*Not estimated*	$\kappa_s = 4.137 \ (\pm0.074)$
	$\kappa_w = 81$		
	$\kappa_a = 1$		
Flow modeling parameters See (2) and (3)[a]	$\mu_w = 1.002 \times 10^{-3}$ Pa s	$\log [k_v \ (\mathrm{m}^2)] = -11.683 \ (\pm0.620)$	$\log [k_v \ (\mathrm{m}^2)] = -11.928 \ (\pm0.243)$
	$\rho_w = 1000$ kg/m^3	$\varphi = 0.233 \ (\pm0.057)$	$\varphi = 0.189 \ (\pm0.030)$
	$k_v/k_h = 0.05$		
Relative permeability and capillary pressure functions. See (4) and (5)[a].	$S_w^{res} = 0.083$	*fixed*	*fixed*
	$S_w^{sat} = 1.0$		
	m = 3.447		
	$\log [\alpha^{-1} \ (\mathrm{Pa})] = 3.45$		
Geostatistical model for log-permeability (spherical semivariogram)[b]	*Horizontal* $c_0 = 0.0, \ c_1 = 0.269, \ r = 20.0$ m	*fixed*	*fixed*
	Vertical $c_0 = 0.0, \ c_1 = 0.269, \ r = 0.8$ m		
Injection flow rate (duration)[c]	$Q_1 = 0.278 \times F$ kg/s (4 h)	$F = 1.03 \ (\pm0.22)$	$F = 1.25 \ (\pm0.10)$
	$Q_2 = 0.165 \times F$ kg/s (6.75 h)		
	$Q_3 = 0.185$ kg/s (6 h)		
	$Q_4 = 0.185$ kg/s (6 h)		
	$Q_5 = 0.185$ kg/s (6 h)		
Boundary conditions	Bottom: free drainage	*fixed*	*fixed*
	Sides: zero flux		
	Top: total flux = 1.0e-4 kg/s		

[a]Parameters defined in text.
[b]As defined in Table 1.
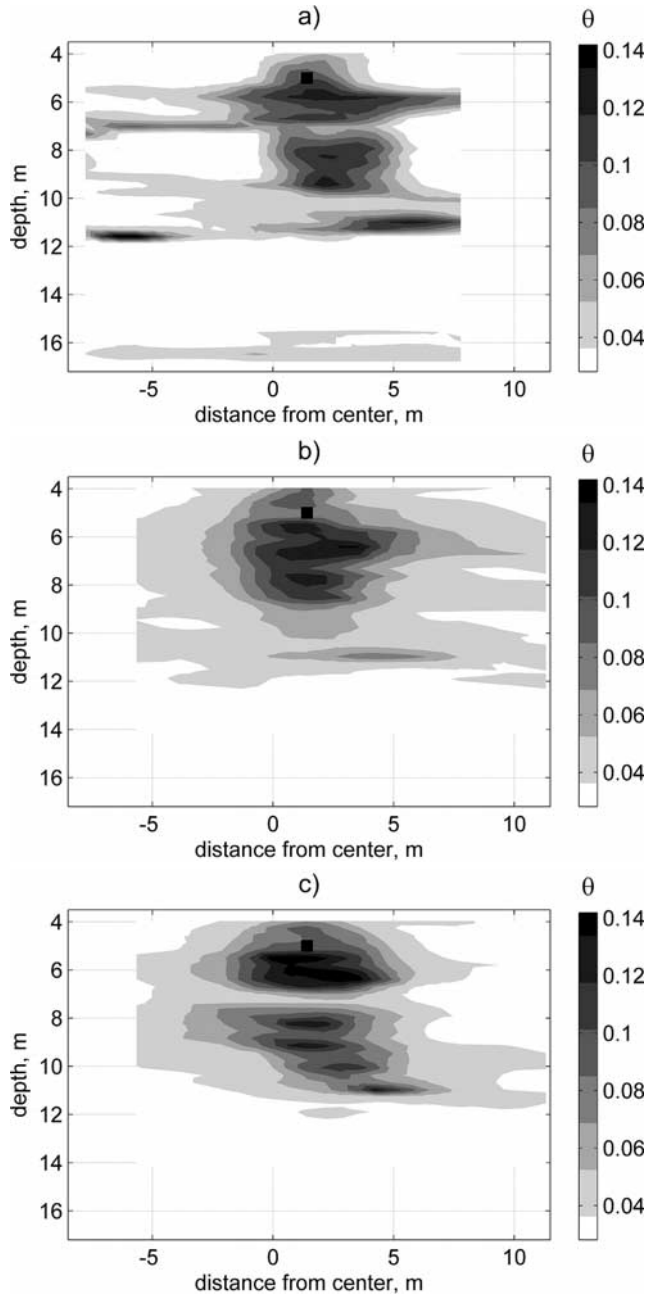[c]F is the factor by which the measured injection flow rate is multiplied.

Figure 15. Comparison of (a) water content (θ) as measured from dense NP data set with predicted distributions given by (b) inversion realization obtained using limited NP data set (using 2 wells at three times), and (c) inversion realization obtained using the GPR data set (collected using 4 GPR wells at two survey times) and the limited NP data set. This figure shows two-dimensional slices (see line AB in Figure 13) from three-dimensional models.

approach for estimating the unknown parameters listed in Table 3, which include the petrophysical parameter κ_s, the porosity, the mean log-permeability, the log-permeability modifier values at 16 pilot point locations, and a factor by which the reported flow rates at the injection point are multiplied. As before, we assume that no prior information is available for the unknown parameters, except for the calculated parameters of the log-permeability semivario-

gram function, yielding the objective function (13) with the first and second terms.

[72] We performed multiple inversion realizations using the data sets described above and with the flow simulation including the first two water injections and continuing up to the time of the second GPR survey (GPR-1) (see Figure 12). The results are summarized in Table 3.

[73] Flow simulations with the three-dimensional models that were obtained through inversion then allowed for the water distributions to be recorded for the time corresponding to NP survey NP-3 (see Figure 12). Multiplying the simulated water saturation values at this time by the estimated porosity values gave predictions of water content, which could be compared with the three-dimensional water content data sets (inferred from interpolation of the dense NP measurements) collected at the same time.

[74] In Figure 15, two-dimensional slices (along the line labeled AB in Figure 13) of the dense NP data set (Figure 15a) are compared to slices of the predicted water content distributions (for a single inversion realization) for two different cases of inversion. The first case (Figure 15b) includes inversion using only the limited NP data sets (i.e., no GPR data were used). The second case (Figure 15c) demonstrates the relative gain from including data from two GPR surveys in the inversion. While the overall trends are similar for both cases, inclusion of GPR measurements allows for various peaks in water content to be predicted more accurately.

[75] To better illustrate this point, vertical profiles of predicted and measured water content at a location near the injection well are given in Figure 16 for the same
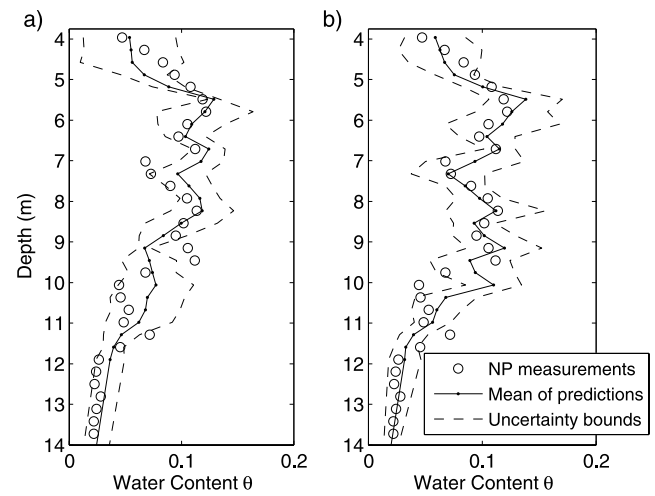

Figure 16. Comparison of water content profile near injection point as measured by dense NP data set (circles) with the mean of the predicted water content profiles (solid line with dots) obtained through inversion of (a) limited NP data set (using 2 wells at three times) and (b) both the GPR data set and the limited NP data set. Note that while NP measurements were collected in 27 wells to obtain the dense NP data sets, only a limited subset of NP measurements were used for inversion (see Figure 13); however, all NP data are used to test the inversion predictions. The dashed lines around the mean of the predicted profiles indicate the estimation uncertainty (±2 standard deviations).

cases. In this figure, the mean of 5 inversion realizations is shown, as are the prediction uncertainty bounds. The parameters that were estimated for both cases are listed in Table 3.

[76] It is worth emphasizing that while NP measurements were collected in 27 wells to obtain the dense NP data sets at eight times, only a limited subset of NP measurements at each time are actually used for inversion (see Figures 12 and 13); however, all NP data were used to test the inversion predictions.

5. Conclusions

[77] It is recognized that subsurface flow and contaminant transport processes are critically affected by the structure and heterogeneity of the subsurface as well as the related distribution of soil moisture. While geophysical methods (such as GPR) may provide high-resolution images of the subsurface, the relation between these images and parameters affecting flow and transport remains ambiguous. On the other hand, while hydrological data contain information about properties relevant to flow and transport, their spatial coverage and resolution is usually insufficient. A joint inversion approach has the potential to combine the strengths of both characterization methods.

[78] A method was described for estimating field-scale soil hydraulic parameters and parameters of the petrophysical function using time-lapse multiple-offset cross-borehole GPR travel times and other hydrological data, such as water content measurements inferred from neutron probe logs. This research builds upon previous work in order to accommodate uncertainty in the petrophysical function and to increase the flexibility of GPR measurement configurations that may be considered, and consequently increase the resolution at which soil hydraulic parameters may be estimated.

[79] The method was applied to two synthetic examples, which consisted of a model with uniform soil hydraulic parameters and a model with heterogeneous permeability. Potential errors in the petrophysical function were observed to significantly affect the soil hydraulic parameter estimates, but inclusion of a petrophysical parameter in the joint inversion procedure allowed for improved estimates of the soil hydraulic parameters.

[80] The importance of accounting for errors in the forward model used for simulating GPR measurements was also addressed. Using the straight-ray approximation to simulate GPR travel times introduces bias in some cases—the travel time bias was spatially dependent and time dependent, showing over-prediction near the edges of the water plume at early times in the injection experiment. To compensate for this bias, an additional correction parameter was estimated during inversion. In heterogeneous models, the bias was minimal, making estimation of the correction parameter unnecessary.

[81] The method was also applied to the U.S. Department of Energy (DOE) Hanford field site in Washington, where time-lapse GPR and NP data sets were collected. Compared to predictions made through inversion of a limited NP data set, inclusion of GPR data in the inversion procedure allowed for soil hydraulic parameter estimates that gave improved predictions of water saturation. We conclude that the approach can provide in a minimally invasive manner accurate estimates of field-scale soil hydraulic parameters and the related moisture distribution.

[82] Future research that is likely to strengthen the joint inversion approach and widen its applicability for the characterization of complex subsurface flow and transport systems includes the following: (1) implementing GPR forward modeling capabilities for additional measurement types (e.g., cross-borehole amplitude and surface reflection data); (2) incorporating capabilities for joint inversion with additional geophysical methods, such as seismic and electrical methods; (3) accounting for spatial variations of the petrophysical function and its dependence on temperature; and (4) exploring the potential of estimating parameters of the spatial correlation functions within the joint inversion procedure. Alternative joint inversion methodologies and different descriptions of geological heterogeneity as applied to the Hanford site experiment may also be explored in the future.

References

Alharthi, A., and J. Lange (1987), Soil water saturation: Dielectric determination, *Water Resour. Res.*, 23, 591–595.

Alumbaugh, D., P. Y. Chang, L. Paprocki, J. R. Brainard, R. J. Glass, and C. A. Rautman (2002), Estimating moisture contents in the vadose zone using cross-borehole ground penetrating radar: A study of accuracy and repeatability, *Water Resour. Res.*, 38(12), 1309, doi:10.1029/2001WR000754.

Annan, P. (2005), GPR methods for hydrogeological studies, in *Hydrogeophysics*, edited by Y. Rubin and S. S. Hubbard, chap. 7, 532 pp., Springer, New York.

Ansoult, M., L. W. DeBacker, and M. Declrercq (1984), Statistical relationship between apparent dielectric constant and water content in porous media, *J. Soil Sci. Soc. Am.*, 48, 47–50.

Archie, G. E. (1942), The electrical resistivity log as an aid in determining some reservoir characteristics, *Trans. Am. Inst. Min. Mat.*, 146, 54–62.

Bergmann, T., J. O. A. Robertsson, and K. Holliger (1998), Finite-difference modeling of electromagnetic wave propagation in dispersive and attenuating media, *Geophysics*, 63(3), 856–867.

Binley, A., P. Winship, R. Middleton, M. Pokar, and J. West (2001), High-resolution characterization of vadose zone dynamics using cross-borehole radar, *Water Resour. Res.*, 37(11), 2639–2652.

Binley, A., G. Cassiani, R. Middleton, and P. Winship (2002), Vadose zone flow model parameterization using cross-borehole radar and resistivity imaging, *J. Hydrol.*, 267, 147–159.

Birchak, J. R., L. G. Gardner, J. W. Hipp, and J. M. Victor (1974), High dielectric constant microwave probes for sensing soil moisture, *Proc. IEEE*, 62(1), 93–98.

Bregman, N. D., R. C. Bailey, and C. H. Chapman (1989), Crosshole seismic tomography, *Geophysics*, 54, 200–215.

Cai, J., and G. A. McMechan (1995), Ray-based synthesis of bistatic ground penetrating radar profiles, *Geophysics*, 60, 87–96.

Casper, D. A., and K.-J. S. Kung (1996), Simulation of ground-penetrating radar waves in a 2-D soil model, *Geophysics*, 61, 1034–1049.

Chan, C. Y., and R. J. Knight (1999), Determining water content and saturation from dielectric measurements in layered materials, *Water Resour. Res.*, 35(1), 85–94.

Daniels, D. J. (1996), *Surface Penetrating Radar*, Inst. of Electr. Eng., London, U.K.

Davis, J. L., and A. P. Annan (1989), Ground-penetrating radar for high-resolution mapping of soil and rock stratigraphy, *Geophys. Prospect.*, 37, 531–551.

Day-Lewis, F. D., and J. W. Lane Jr. (2004), Assessing the resolution-dependent utility of tomograms for geostatistics, *Geophys. Res. Lett.*, *31*, L07503, doi:10.1029/2004GL019617.

de Loor, G. P. (1964), Dielectric properties of heterogeneous mixtures, *Appl. Sci. Res.*, *B3*, 479–482.

Deutsch, C. V., and A. G. Journel (1992), *GSLIB: Geostatistical Software Library and User's Guide*, Oxford Univ. Press, New York.

Dobson, M. C., F. T. Ulaby, M. T. Hallikainen, and M. A. El-Rayes (1985), Microwave dielectric behavior of wet soils—Part II: Dielectric mixing models, *IEEE Trans. Geosci. Remote Sens.*, *32*(1), 35–46.

Eppstein, M. J., and D. E. Dougherty (1998), Efficient three-dimensional data inversion: Soil characterization and moisture monitoring from cross-well ground-penetrating radar at a Vermont test site, *Water Resour. Res.*, *34*(8), 1889–1900.

Fares, A., P. Buss, M. Dalton, A. I. El-Kadi, and L. R. Parsons (2004), Dual field calibration of capacitance and neutron soil water sensors in a shrinking–swelling clay soil, *Vadose Zone J.*, *3*, 1390–1399.

Fayer, M. J., J. B. Sisson, W. A. Jordan, A. H. Lu, and P. R. Heller (1993), Subsurface injection of radioactive tracers: Field experiment for model validation testing, *NUREG/CR-5996*, U.S. Nucl. Regul. Comm., Washington, D. C.

Fayer, M. J., R. E. Lewis, R. E. Engleman, A. L. Pearson, C. J. Murray, J. L. Smoot, R. R. Randall, W. H. Wegener, and A. H. Lu (1995), Re-evaluation of a subsurface injection experiment for testing of flow and transport models, *Rep. PNL-10860*, Pac. Northwest Natl. Lab., Richland, Wash.

Finsterle, S. (1999), iTOUGH2 user's guide, *Rep. LBNL-40040*, Lawrence Berkeley Natl. Lab., Berkeley, Calif.

Freeman, E. J., R. Khaleel, and P. R. Heller (2001), A catalog of vadose zone hydraulic properties for the Hanford site, *Rep. PNNL-13672*, Pac. Northwest Natl. Lab., Richland, Wash.

Friedman, S. P. (1998), A saturation degree-dependent composite spheres model for describing the effective dielectric constant of unsaturated porous media, *Water Resour. Res.*, *34*(11), 2949–2961.

Gee, G. W., and A. L. Ward (2001), Vadose Zone Transport Field Study, *Rep. PNNL-13982*, Pac. Northwest Natl. Lab., Richland, Wash.

Gomez-Hernandez, J. J., A. Sahuquillo, and J. E. Capilla (1997), Stochastic simulation of transmissivity fields conditional to both tranmissivity and piezometric data—1, Theory, *J. Hydrol.*, *203*, 162–174.

Hubbard, S. S., Y. Rubin, and E. Majer (1997), Ground-penetrating-radar assisted saturation and permeability estimation in bimodal systems, *Water Resour. Res.*, *33*, 971–990.

Huisman, J. A., S. S. Hubbard, J. D. Redman, and A. P. Annan (2003), Measuring soil water content with ground penetrating radar: A review, *Vadose Zone J.*, *2*, 476–491.

Hunt, A. G., and G. W. Gee (2002), Water-retention of fractal soil models using continuum percolation theory: Tests of Hanford site soils, *Vadose Zone J.*, *1*, 252–260.

Hyndman, D. W., and S. M. Gorelick (1996), Estimating lithological and transport properties in three dimensions using seismic and tracer data, the Kesterson aquifer, *Water Resour. Res.*, *32*(9), 2659–2670.

Hyndman, D. W., J. M. Harris, and S. M. Gorelick (1994), Coupled seismic and tracer test inversion for aquifer property characterization, *Water Resour. Res.*, *30*(7), 1965–1977.

Jacobsen, O. H., and P. Schjonning (1993), A laboratory calibration of time domain reflectometry for soil water measurement including effects of bulk soil density and texture, *J. Hydrol.*, *151*, 147–157.

Jury, W. A., D. Russo, G. Sposito, and H. Elabd (1987), The spatial variability of water and solute transport properties in unsaturated soil: I. Analysis of property variation and spatial structure with statistical models, *Hilgardia*, *55*, 1–32.

Kowalsky, M. B. (2003), Characterization approaches using ground-penetrating radar and hydrological measurements in variably saturated porous media, Ph.D. dissertation, 194 pp., Univ. of Calif., Berkeley.

Kowalsky, M. B., P. Dietrich, G. Teutsch, and Y. Rubin (2001), Forward modeling of ground-penetrating radar data using digitized outcrop images and multiple scenarios of water saturation, *Water Resour. Res.*, *37*(6), 1615–1626.

Kowalsky, M. B., S. A. Finsterle, and Y. Rubin (2004a), Estimating flow parameter distributions using ground-penetrating radar and hydrological measurements during transient flow in the vadose zone, *Adv. Water Resour.*, *27*(6), 583–599.

Kowalsky, M. B., Y. Rubin, and P. Dietrich (2004b), The use of ground-penetrating radar for characterizing sediments under transient flow conditions, in *Aquifer Characterization*, edited by J. S. Bridge and D. W. Hyndman, *SEPM Spec. Publ.*, *80*, 107–127.

Kunz, K. S., and R. J. Luebbers (1993), *The Finite Difference Time Domain Method for Electromagnetics*, CRC Press, Boca Raton, Fla.

Lambot, S., M. Antoine, I. van den Bosch, E. C. Slob, and M. Vanclooster (2004), Electromagnetic inversion of GPR signals and subsequent hydro-dynamic inversion to estimate effective vadose zone hydraulic properties, *Vadose Zone J.*, *3*, 1072–1081.

Last, G. V., and T. G. Caldwell (2001), Core sampling in support of the Vadose Zone Transport Field Study, *Rep. PNNL-13454*, Pac. Northwest Natl. Lab., Richland, Wash.

Last, G. V., T. G. Caldwell, and A. T. Owen (2001), Sampling of boreholes WL-3A through -12 in support of the Vadose Zone Transport Field Study, *Rep. PNNL-13631*, Pac. Northwest Natl. Lab., Richland, Wash.

Lesmes, D. P., and S. P. Friedman (2005), Relationships between the electrical and hydrogeological properties of rocks and soils, in *Hydrogeophysics*, edited by Y. Rubin and S. S. Hubbard, chap. 4, 532 pp., Springer, New York.

Levenberg, K. (1944), A method for the solution of certain problems in least squares, *Q. Appl. Math.*, *2*, 164–168.

Majer, E. L., J. E. Peterson, K. H. Williams, T. M. Daley, and G. Gee (2000), High resolution of vadose zone transport using crosswell radar and seismic methods, *Rep. PNNL-13791*, Pac. Northwest Natl. Lab., Richland, Wash.

Marquardt, D. (1963), An algorithm for least squares estimation of non-linear parameters, *SIAM J. Appl. Math.*, *11*, 431–441.

Martinez, A., and A. P. Byrnes (2001), Modeling dielectric-constant values of geologic materials: An aid to ground-penetrating radar data collection and interpretation, *Curr. Res. Earth Sci., Bull.*, *247*, part 1, 1–16.

McLaughlin, D., and L. R. Townley (1996), A reassessment of the ground-water inverse problem, *Water Resour. Res.*, *32*(5), 1131–1161.

Moysey, S., and R. Knight (2004), Modeling the field-scale relationship between dielectric constant and water content in heterogeneous system, *Water Resour. Res.*, *40*, W03510, doi:10.1029/2003WR002589.

Moysey, S., K. Singha, and R. Knight (2005), Inferring field-scale rocks physics relationships through numerical simulation, *Geophys. Res. Lett.*, *32*, L08304, doi:10.1029/2004GL022152.

Or, D., and J. M. Wraith (1999), Temperature effects on soil bulk dielectric permittivity measured by time domain reflectometry: A physical model, *Water Resour. Res.*, *35*(2), 371–383.

Persson, M., B. Sivakumar, R. Berndtsson, O. H. Jacobsen, and P. Schjonning (2002), Predicting the dielectric constant-water content relationship using artificial neural networks, *Soil Sci. Soc. Am. J.*, *66*, 1424–1429.

Peterson, J. E. (2001), Pre-inversion corrections and analysis of radar to-mographic data, *J. Environ. Eng. Geophys.*, *6*(1), 1–18.

Peterson, J. E., B. N. P. Paulsson, and T. V. McEvilly (1985), Applications of algebraic reconstruction techniques to crosshole seismic data, *Geophysics*, *50*, 1566–1580.

Philip, J. R. (1991), Horizontal Redistribution with capillary hysteresis, *Water Resour. Res.*, *27*(7), 1459–1469.

Pruess, K., C. Oldenburg, and G. Moridis (1999), TOUGH2 user's guide, version 2.0, *Rep. LBNL-43134*, Lawrence Berkeley Natl. Lab., Berkeley, Calif.

RamaRao, B. S., G. de Marsily, and M. G. Marietta (1995), Pilot point methodology for automated calibration of an ensemble of conditionally simulated transmissivity fields: 1. Theory and computational experiments, *Water Resour. Res.*, *31*(3), 475–493.

Ramirez, A., W. Daily, A. Binley, and G. W. Gee (2001), Final report, FY 2001, 200 East Vadose test site Hanford, Washington, electrical resistance tomography, *Rep. PNNL-13794*, Pac. Northwest Natl. Lab., Richland, Wash.

Robinson, D. A., S. B. Jones, J. M. Wraith, D. Or, and S. P. Friedman (2003), Advances in dielectric and electrical conductivity measurement using time domain reflectometry: Simultaneous measurement of water content and bulk electrical conductivity in soils and porous media, *Vadose Zone J.*, *2*, 444–475.

Robinson, D. A., M. G. Schaap, D. Or, and S. B. Jones (2005), On the effective measurement frequency of time domain reflectometry in dispersive and nonconductive dielectric materials, *Water Resour. Res.*, *41*, W02007, doi:10.1029/2004WR003816.

Rockhold, M. L., C. J. Murray, and M. J. Fayer (1999), Conditional simulation and upscaling of soil properties, in *Proceedings of the International Workshop on Characterization and Measurement of the Hydraulic Properties of Unsaturated Porous Media*, edited by M. T. van Genuchten, F. J. Leij, and L. Wu, pp. 1391–1402, Univ. of Calif., Riverside.

Roth, K. R., R. Schulin, H. Fluhler, and W. Attinger (1990), Calibration of time domain reflectometry for water content measurement using a composite dielectric approach, *Water Resour. Res.*, *26*, 2267–2273.

Rubin, Y. (2003), *Applied Stochastic Hydrogeology*, Oxford Univ. Press, New York.

Rucker, D. F., and T. P. A. Ferré (2004), Parameter estimation for soil hydraulic properties using zero-offset borehole radar: Analytical method, *Soil Sci. Soc. Am. J.*, *68*, 1560–1567.

Russo, D., and M. Bouton (1992), Statistical analysis of spatial variability in unsaturated flow parameters, *Water Resour. Res.*, *28*, 1911–1925.

Schaap, M. G., P. J. Shouse, and P. D. Meyer (2003), Laboratory measurements of the unsaturated hydraulic properties at the Vadose Zone Transport Field Study site, *Rep. PNNL-14284*, Pac. Northwest Natl. Lab., Richland, Wash.

Sethian, J. A., and A. M. Popovici (1999), 3-D travel time computation using the fast marching method, *Geophysics*, *64*(2), 516–523.

Sihvola, A. (1999), *Electromagnetic Mixing Formulas and Applications*, *IEEE Electromagn. Waves Ser. 47*, Inst. of Electr. Eng., London, U.K.

Sisson, J. B., and A. H. Lu (1984), Field calibration of computer models for applications to buried liquid discharges: A status report, *Tech. Rep. RHO-ST-46-P*, Rockwell Hanford Oper., Richland, Wash.

Smoot, J. L., and A. H. Lu (1994), Interpretation and modeling of a subsurface injection test, 200 East Area, Hanford, Washington, in *Thirty-Third Hanford Symposium on Health and the Environment, In-Situ Remeditaion: Scientific Basis for Current and Future Technologies*, edited by G. W. Gee and N. R. Wing, Pac. Northwest Natl. Lab., Richland, Wash.

Smoot, J. L., and R. E. Williams (1996), A geostatistical methodology to assess the accuracy of unsaturated flow models, *NUREG/CR-6411*, U.S. Nucl. Regul. Comm., Washington, D. C.

Stewart, R. R. (1991), *Exploration Seismic Tomography: Fundamentals*, *Course Notes Ser.*, vol. 3, 140 pp., Soc. of Explor. Geophys., Tulsa, Okla.

Topp, G. C., J. L. Davis, and A. P. Annan (1980), Electromagnetic determination of soil water content: Measurements in coaxial transmission lines, *Water Resour. Res.*, *16*(3), 574–582.

van Genuchten, M. T. (1980), A closed-form equation for predicting the hydraulic conductivity of unsaturated soils, *Soil Sci. Soc. Am. J.*, *44*, 892–898.

Ward, A. L., T. G. Caldwell, and G. W. Gee (2000), Vadose Zone Transport Field Study: Soil water content distributions by neutron moderation, *Rep. PNNL-13795*, Pac. Northwest Natl. Lab., Richland, Wash.

Yao, T., P. J. Wierenga, A. R. Graham, and S. P. Neuman (2004), Neutron probe calibration in a vertically stratified vadose zone, *Vadose Zone J.*, *3*, 1400–1406.

Zhang, Z. F., A. L. Ward, and G. W. Gee (2004), A combined parameter scaling and inverse technique to upscale the unsaturated hydraulic parameters for heterogeneous soils, *Water Resour. Res.*, *40*, W08306, doi:10.1029/2003WR002925.

S. Finsterle, S. Hubbard, M. B. Kowalsky, E. Majer, and J. Peterson, Earth Sciences Division, Lawrence Berkeley National Laboratory, Berkeley, CA 94720, USA. (mbkowalsky@lbl.gov)

G. Gee and A. Ward, Hydrology Group, Pacific Northwest National Laboratory, Richland, WA 99353, USA.

Y. Rubin, Department of Civil and Environmental Engineering, University of California, Berkeley, CA 94720-1710, USA.